AFRL-RX-WP-TP-2008-4341

ATHERMAL MECHANISMS OF SIZE-DEPENDENT CRYSTAL FLOW GLEANED FROM THREE-DIMENSIONAL DISCRETE DISLOCATION SIMULATIONS (PREPRINT)

S.I. Rao, D.M. Dimiduk, T.A. Parthasarathy, M.D. Uchic, M. Tang, and C. Woodward

UES, Inc.

JANUARY 2008

AIR FORCE RESEARCH LABORATORY
MATERIALS AND MANUFACTURING DIRECTORATE
WRIGHT-PATTERSON AIR FORCE BASE, OH 45433-7750
AIR FORCE MATERIEL COMMAND
UNITED STATES AIR FORCE

REPORT DOCUMENTATION PAGE

Form Approved
OMB No. 0704-0188

1. REPORT DATE *(DD-MM-YY)*	2. REPORT TYPE	3. DATES COVERED *(From - To)*
January 2008	Journal Article Preprint	

4. TITLE AND SUBTITLE

ATHERMAL MECHANISMS OF SIZE-DEPENDENT CRYSTAL FLOW GLEANED FROM THREE-DIMENSIONAL DISCRETE DISLOCATION SIMULATIONS (PREPRINT)

5a. CONTRACT NUMBER
FA8650-04-D-5233

5b. GRANT NUMBER

5c. PROGRAM ELEMENT NUMBER
62102F

6. AUTHOR(S)

S.I. Rao and T.A. Parthasarathy (UES, Inc.)
D.M. Dimiduk and M.D. Uchic (AFRL/RXLM)
M. Tang (Lawrence Livermore National Laboratory)
C. Woodward (Northwestern University)

5d. PROJECT NUMBER
2311

5e. TASK NUMBER
00

5f. WORK UNIT NUMBER
23110002

7. PERFORMING ORGANIZATION NAME(S) AND ADDRESS(ES)

UES, Inc.
4401 Dayton-Xenia Road
Dayton, OH 45432-1894

Metals Branch (AFRL/RXLM)
Metals, Ceramics, and NDE Division
Materials and Manufacturing Directorate
Wright-Patterson Air Force Base, OH 45433-7750
Air Force Materiel Command, United States Air Force

Lawrence Livermore National Laboratory

Northwestern University

8. PERFORMING ORGANIZATION REPORT NUMBER

9. SPONSORING/MONITORING AGENCY NAME(S) AND ADDRESS(ES)

Air Force Research Laboratory
Materials and Manufacturing Directorate
Wright-Patterson Air Force Base, OH 45433-7750
Air Force Materiel Command
United States Air Force

10. SPONSORING/MONITORING AGENCY ACRONYM(S)
AFRL/RXLM

11. SPONSORING/MONITORING AGENCY REPORT NUMBER(S)
AFRL-RX-WP-TP-2008-4341

12. DISTRIBUTION/AVAILABILITY STATEMENT
Approved for public release; distribution unlimited.

13. SUPPLEMENTARY NOTES
Journal article submitted to *Acta Materialia*. PAO Case Number: WPAFB 07-0679; Clearance Date: 11 Dec 2007. The U.S. Government is joint author of this work and has the right to use, modify, reproduce, release, perform, display, or disclose the work.

14. ABSTRACT

Recent experimental studies discovered that micrometer-scale face-centered cubic crystals show strong strengthening effects, even at high initial dislocation densities. We use large-scale 3-D discrete dislocation simulations (DDS) to explicitly model the deformation behavior of FCC Ni microcrystals in the size rang 0.5 to 20 μm. The study shows that two size-sensitive a thermal hardening processes, beyond forest hardening, are sufficient to develop the dimensional scaling of the flow stress, stochastic stress variation, flow intermittency and, high initial strain-hardening rates, similar to experimental observations for various materials. One mechanism, source-truncation hardening, is especially potent in micrometer-scale volumes. A second mechanism, termed exhaustion hardening, results from a breakdown of the mean-field conditions for forest hardening in small volumes, thus biasing the statistics of ordinary dislocation processes.

15. SUBJECT TERMS
dislocation synamics, plastic deformation, compression test, nickel, size effects

16. SECURITY CLASSIFICATION OF:			17. LIMITATION OF ABSTRACT:	18. NUMBER OF PAGES	19a. NAME OF RESPONSIBLE PERSON (Monitor)
a. REPORT	b. ABSTRACT	c. THIS PAGE			John H. Barnes
Unclassified	Unclassified	Unclassified	SAR	40	19b. TELEPHONE NUMBER *(Include Area Code)* N/A

Standard Form 298 (Rev. 8-98)
Prescribed by ANSI Std. Z39-18

Athermal mechanisms of size-dependent crystal flow gleaned from three-dimensional discrete dislocation simulations

S.I. Rao,* D.M. Dimiduk, T.A. Parthasarathy,* M.D. Uchic, M. Tang,[#] and C. Woodward[^]

Air Force Research Laboratory, Materials and Manufacturing Directorate, AFRL/MLLM
Wright-Patterson AFB, OH 45433-7817

*UES, Inc., 4401 Dayton-Xenia Rd, Dayton, OH 45432-1894

[#]Lawrence Livermore National Laboratory, P.O. Box 808, L-45 Livermore, CA 94551

[^]Northwestern University, Department of Materials Science and Engineering, 2220 Campus Drive, Evanston, IL 60208-3108

Keywords: dislocation dynamics, plastic deformation, compression test, nickel, size effects

ABSTRACT

Recent experimental studies discovered that micrometer-scale face-centered cubic crystals show strong strengthening effects, even at high initial dislocation densities. We use large-scale 3-D discrete dislocation simulations (DDS) to explicitly model the deformation behavior of FCC Ni microcrystals in the size range 0.5 – 20 μm. The study shows that two size-sensitive athermal hardening processes, beyond forest hardening, are *sufficient* to develop the dimensional scaling of the flow stress, stochastic stress variation, flow intermittency and, high initial strain-hardening rates, similar to experimental observations for various materials. One mechanism, source-truncation hardening, is especially potent in micrometer-scale volumes. A second mechanism, termed exhaustion hardening, results from a break-down of the mean-field conditions for forest hardening in small volumes, thus biasing the statistics of ordinary dislocation processes.

1 INTRODUCTION

Experimental microcompression studies confirm that dislocation plasticity of single-phase single crystals is strongly influenced by their physical size [1-8]. While selected details of specific specimen and testing parameters affect the quantitative response, the stress-strain flow behavior is qualitatively characterized by four distinct attributes: i) a sharply rising flow stress with decreasing sample size that follows power-law scaling, having a scaling exponent ranging from approximately -0.4 to -1.0; ii) stochastic variation in the measured flow stress that exhibits wider scatter at smaller sample sizes; iii) intermittency in plastic flow as revealed by either repeated load drops or constant-stress flow avalanches, depending upon the testing mode; and iv) an extended (> 1% strain) elastic-plastic flow transition characterized by an average strain-hardening rate, $\Theta > G/200$, where G is the shear modulus. As might also be expected, there has been a flurry of reports that purport to explain these findings from the behavior of dislocations

via theory or simulation [3, 5, 9-19]. However, none of these theory or simulation studies even qualitatively depicts the aforementioned characteristic experimental findings, particularly for the microcrystals known to contain a large initial dislocation density [20]. Thus, the present study was focused on examining selected aspects of these characteristic features of microcrystal deformation using the 3d discrete dislocation simulation (DDS) technique [21-27].

While structuring the present study, consideration was given not only to prior 3d DDS investigations of sample size effects, but also to selected expectations for size-affected flow from forest-hardening theory. Both theoretical and experimental studies confirm the mean-field forest-hardening law, $\tau^* \propto \sqrt{\rho_f}$, where τ^* is the flow stress and ρ_f is the forest-dislocation density [28-31]. Further, the mean-field theory contains a characteristic dimension, $\lambda_f = 1/\sqrt{\rho_f}$ and, the flow-stress proportionality is shown to hold over more than four orders-of-magnitude, from about 10 nm to nearly 100 μm [29]. However, deformation of small volumes is expected to violate the mean-field assumption. Also, studies consistently show that λ_f is <u>not</u> the explicit controlling length. Rather, another scale exists that may be at least one-order-of-magnitude larger and better relates to a "mean-free-path" or a "correlation length" for glide resistance [28, 30, 31]. The later parameter takes on fundamental importance to the deformation of a small material volume, regardless of whether the size is set by free surfaces or other constraints [32-36].

Gil Sevillano, et. al. directly developed a definition of the single-slip glide-resistance correlation length, $\xi \approx 8.5/\sqrt{\rho_o/10}$, from 2d simulations of single-dislocation percolation through point-obstacle fields [35, 36]. Subsequently, predictions for the size-dependence of τ^* from Gil Sevillano, et. al., were phenomenologically validated through deformation of microcrystals containing dislocation densities ranging from $\sim 10^{12}/m^2$ to $\sim 10^{13}/m^2$ but, having varying diameters at or below the expected correlation lengths [3]. While this report implies that the agreement between the model of Gil Sevillano, et. al., and microcrystal deformation experiments was perhaps fortuitous, significant merit remains within their treatment.

The more general question of what is the 3d glide-resistance correlation length, ξ^*, and what are the kinetic attributes of a 3d dislocation ensemble that set the glide resistance as a function of sample dimensions remain unsolved. While selected 3d discrete dislocation simulation (DDS) studies (using periodic boundary conditions) confirmed the basic framework of the forest-hardening law and, suggested new dislocation mechanisms for forest hardening [21-25], the technique has not provided quantitative definition of ξ^*. Indeed any thorough attempt at such 3d analysis would rank among the so-called "grand challenge" computing problems, requiring numerous simulations using a scalable parallel code. Such simulations must either break the commonly employed periodic boundary conditions or perhaps, employ periodic boundaries on selective simulation cells that permit dislocation motion on the scale of the correlation length without cell-boundary interactions. Nonetheless, either a 3d DDS-based substitute for or, a 3d confirmation of the established 2d relationships and associated approximations for ξ^*, forms an essential basis for understanding plasticity at small scales.

There have been initial 3d DDS studies of the material size effects on strength for dislocations in small volumes [17, 18, 37]. Blanckenhagen, et. al., used 3d DDS to model deformation of a columnar-grained film of thickness = diameter < ~1 μm [37]. The results extended their earlier 2d DDS findings [38] showing that impenetrable boundaries (grain boundaries) within a film can set a new characteristic length when Frank-Read (FR) sources become single-arm or spiral sources within the volume. The new sources are formed when initial source lengths exceed a dimension that is ~1/3 the constrained grain or film thickness [38, 39]. The studies found that the flow stress, τ^*, scales as $1/D$, where D is the film thickness or grain size, because of the scaling of source length with cell size.

Weygand, et. al., [17] used 3d DDS to model the deformation of Al-like simulation cells in the size range 0.5 – 1 μm, having an initial dislocation source density of $2.1 \times 10^{13}/m^2$, a nominal strain rate of $5 \times 10^3/s$ and a height-to-width ratio (L/D) of 2. They obtained a power law for τ^* scaling with sample size, D, having an exponent of -0.6, which is similar to that found for a wide set of experiments over a much large size range [8].

Tang, et. al., [18] also used 3d DDS to study compression deformation of simulation cells in the size range 0.3 – 1.6 μm, having $L/D = 3$, under a high strain rate of $-6.66 \times 10^5/s$ applied along the {001} orientation. They found that FR sources frequently become single-arm sources, the τ^* for the simulation cells increases with decreasing size following a $1/D$ scaling relationship and, dislocation escape at free surfaces is important.

From the preceding summary, it is clear that there is a large gap between what has been accomplished via the 3d DDS technique and the open questions pertaining to size-dependent strengthening and flow. No simulation study has examined cell sizes substantially larger that 1 μm, micromechanisms of strengthening are inadequately described, strain-rate effects are unexplored and even the findings about the scaling of τ^* with cell dimensions are inconclusive. Thus, the present DDS studies examined a wider range of cell sizes that more closely approach the 2d estimates for ξ^* from the established forest-hardening theory. As with any simulation technique there remains significant restrictions on the level of "realism" that can be achieved irrespective of computing capacity. Nonetheless, examining the results from simulations and comparing them to appropriate experiments identified key mechanistic factors that are sufficient to rationalize much of the athermal size-affected strengthening in FCC microcrystals.

The remainder of this manuscript is organized as follows: 1) descriptions are provided for the simulation technique, including the 3d DDS method, selection of simulation cells, initial conditions, loading scheme and strain rate. 2) Simulation results are described for the behavior of Ni-like simulation cells for an initial dislocation source density of $2 \times 10^{12}/m^2$. These results introduce the dislocation configurations for strengthening of microcrystals. Subsequently, results are presented from strain-rate change simulations and simulation cells of varying initial dislocation densities. 3) A discussion ensues that presents microcrystal strengthening as mechanistically consisting of principally three components, qualitatively relates these results to ξ^* and, emphasizes the importance of stochastic effects on the proportional limit, τ^* and τ^* scaling with sample size. 4) From there the discussion turns to the implications of the present work on selected prior studies and, to descriptions of open issues. 5) The descriptions are followed by a brief summary of the study and selected conclusions.

2 SIMULATION TECHNIQUE

A version of the 3-dimensional parallel dislocation dynamics simulator, ParaDiS [26, 27], developed at Lawrence Livermore National Laboratory, was used to simulate the stress-strain response of micron-sized crystals to small strains (~1%). A detailed description of the technique, elastic constants and velocity law used, treatment of surface boundary conditions (simple surface approximation or SSA), are given in a previous publication [19]. Here, we describe only the initial cell geometries, the initial dislocation microstructure introduced into the simulation cells and the simulated loading schemes. Further descriptions and rationale for the parameters selected may be found in the appendix Rationale for Simulation Choices.

Simulation Cell Geometries and Slip Systems

The simulations used both cubic cells having edge lengths a_o = 10 and 20 μm and, tetragonal cells that approximately mimic the cylindrical specimens used in experiments. Noting that the 'sample size' of interest is the slip plane dimension, it is easily shown that for single slip orientations, approximating a cylindrical specimen will require the diagonal of the face of the tetragonal cell to be equal to the diameter of the cylinder. For the tetragonal cells, the length along the [001] axes was taken to be 2.83 times the diagonal on the (001) plane face, which was a [110] or a $[1\bar{1}0]$ direction. The length of that face diagonal was varied from 0.5 to 10 μm. The surfaces of the simulation cell were along <001> type axes while the load was imposed along the $[4\bar{1}3]$ (nominally single-slip) crystal direction. The $(\bar{1}\bar{1}1)[110]$ slip system is maximally stressed under these conditions, having a Schmidt factor of 0.47. Two other slip systems were highly stressed, those being the $(\bar{1}\bar{1}1)[0\bar{1}1]$ and $(1\bar{1}1)[\bar{1}10]$, both having a Schmidt factor of 0.37.

At large sizes, 10 and 20 μm cubic cells were used in the simulations to decrease the computer time required for the large-scale simulations relative to the tetragonal simulation cells. For the 10 μm case, at an initial dislocation source density of $2 \times 10^{12}/m^2$, two tetragonal-cell simulation cells were also used. Comparison of critical-stress results from such simulations with results from 10 μm cubic-cell simulations having an identical initial dislocation source density, showed that the 10 μm tetragonal and cubic cells give similar results (within 5%).

Initial Source Configurations and Methods

Initial simulations were run using only a single FR source in a 1 μm cubic cell. Those simulations suggested that for small simulation cells, FR sources become single-arm sources when an expanding dislocation loop intersects a free surface [19]. However, the experimental microcrystals initially contain a 3d network of dislocations as a result of the specimen preparation procedures [3-6]. Also, the initial dislocation density in the experimental microcrystals may range from $5 \times 10^{12}/m^2 - 5 \times 10^{13}/m^2$ [3, 40-42]. As a result, we approximate the initial dislocation configuration with a population of FR sources with each source being pinned at both ends (see appendix) [43]. The spatial

arrangement of FR sources is taken to be random, completely contained within the simulation cell (double-ended sources) and, randomly distributed on the 12 slip systems.

The maximum distance from a pinning point to the surface was approximated as the diameter of the specimen. Therefore, for the majority of the simulations described here, the lengths of the FR sources were taken uniformly random having magnitudes between 0 to $a_o\sqrt{2}$. The initial line direction of the dislocation sources was taken to be random, ranging from 0 to 360 degrees in character, where 0 corresponds to the screw-character direction. Three different initial dislocation source densities were considered, ~7 x $10^{11}/m^2$, 2 x $10^{12}/m^2$ and $10^{13}/m^2$. Table 1 gives the number of simulations performed at each size for the three different starting dislocation source densities, as well as the initial number of sources introduced for each of the simulations. As shown, there is significant scatter in the critical stress results for 0.5, 1 and 4 μm cells from one random arrangement to another, similar to what is observed experimentally. However, for the 10 and 20 μm crystals, the scatter in the critical stresses from one random arrangement to another is fairly small, within 5%.

Simulated Loading Schemes

Two aspects of sample loading were studied; in one the experimental conditions were simulated and in another strain-rate changes were examined. In the experiments a constant displacement rate was prescribed [3]. If at a time step, the specimen plastic displacement rate was lower than the applied rate, the applied stress was incremented to obey a constant applied rate, i.e., for $\delta\varepsilon_p/\delta t < \delta\varepsilon/\delta t$, $\delta\varepsilon_p/\delta t + \delta\varepsilon_e/\delta t = \delta\varepsilon/\delta t$, where ε_p, ε_e and ε are the plastic strain, elastic strain and total strain, respectively. However, if the plastic displacement rate was higher than that of the programmed rate, the applied stress was kept constant, i.e., $\delta\varepsilon_p/\delta t > \delta\varepsilon/\delta t$, $\delta\sigma = 0$. Once the $\delta\sigma = 0$ condition is satisfied, increments in stress occurred only after it was determined that the total displacement at a particular time was less than the applied displacement rate multiplied by the elapsed time, i.e., $\varepsilon_p + \varepsilon_e < \delta\varepsilon/\delta t \ (\Delta t)$. In the simulations the applied external stress was assumed to be uniformly distributed over the volume of the simulation cell.

Nearly all of the simulations were done using a nominal strain rate of 50/s while adhering to the experiment-like loading mode. Selected strain-rate-change tests were also simulated with the 20 μm cubic cells. The 20 μm cells having initial dislocation source densities of 7 x $10^{11}/m^2$ and 2 x $10^{12}/m^2$ and, strained in the nearly-elastic portion of flow at a rate of 50/s, were interrupted and deformed further at a strain rate of 10/s. The critical stress for uninterrupted plastic flow at the lower strain rate was compared with the critical stress obtained when there was no interruption of strain rate, i.e. deformed continuously at a strain rate of 50/s. These results were used to quantify the effect of applied strain rate on the critical-stress results at the 20 μm size.

3 RESULTS

MICROCRYSTAL SIMULATIONS: INITIAL DISLOCATION DENSITY OF 2 x $10^{12}/m^2$

A 3d dislocation viewer, ParaView [44], was modified to examine the 3d dislocation configurations at different stages of the plastic deformation process in the simulations.

Figure 1 gives a snapshot of each of the dislocation microstructures in 1, 4, 10 and 20 μm simulation cells, all at an initial dislocation source density of 2 x $10^{12}/m^2$. From Fig. 1, it is clear that as the size of the simulation cell increases, the number of dislocation segments involved in the calculations increases significantly.

Simulated Stress-Strain Curves, 1 μm Cells

The stress-strain curves obtained on 1 μm tetragonal cells for 8 different initial random seeds, are shown in Fig. 2a. To allow comparison to experimental data, the simulated stress-strain curves were scaled to a shear modulus of 78.7 GPa (59.9 GPa used in simulations). A result from simulating only a single FR source in a 1 μm cell is also shown for comparison in Fig. 2b. In these 1 μm cell simulations, each operating FR sources become a pair of single-end-pinned sources (source-truncation hardening mechanism) at small strains [15, 19, 38]. The simulation that set the lower bound on the distribution of flow stresses (140 MPa), showed a stress-strain curve that exhibited a linear-elastic, perfectly-plastic response, similar to the behavior of simulations of a single FR source, at similar stress levels.

The other seven simulations exhibited flow curves where stress rises incrementally with strain and which end with a saturation flow stress and break-away strain. These also exhibited a significant scatter in the magnitude of the saturation flow stress. This behavior produced flow-curve distributions having generally larger saturation stresses (i.e., 330 MPa in Fig. 3a). In this work, and in prior work, we call this strain-hardening as "exhaustion hardening."

Stress-Strain Curves, Larger Cells and Stress Scaling

Several additional simulations were carried out using the same initial dislocation source density and multiple FR sources for larger simulation cells. Selected stress-strain curves (2 out of 3 different random arrangements for the 4 μm cell, and 1 out of two different arrangements for the 10 and 20 μm cells) are shown in Fig. 3a. These simulation results may be compared with the experimental results obtained over a similar range of sample sizes and shown in Fig. 3b. One may observe in Fig. 3, that the flow stress, both for simulation and experiment, drops rapidly with sample size. Moreover, all of the simulations exhibit an incrementally rising flow curve with plastic strain at the plastic transient, indicative of the exhaustion-hardening phenomenon. The simulated stress-strain curves for the larger 4 and 10 μm cells also reveal overall hardening rates that are much lower than those for the 1 μm simulation cells for the initial period of plastic straining.

Figure 4 compares the critical-stress versus sample-size results for the 3d simulations and experiments [1-6]. The critical stress is scaled by the shear modulus ($\{0.5[C_{11}-C_{12}]C_{44}\}^{1/2}$, where C_{11}, C_{12} and C_{44} are the cubic single-crystal elastic constants, and normalized to the Burger's vector of Ni, i.e. $\tau_{cr}/G*b_{ni}/b_{au,}$ where b_{au} is the Burger's vector magnitude for the alloy (Ni, Au). For the simulations, the critical stress is defined as the primary slip Schmid factor multiplied by the engineering stress at ~1% total strain.

Examination of Dislocation Configurations

Through inspection of the dislocation structure at various positions along the stress-strain curves for all of the simulations, it was possible to identify two primary size-dependent mechanisms of microcrystal strengthening. The first of these, a source-truncation mechanism, was also identified via single-source simulations and a complete description of that mechanism has been published elsewhere [15, 19] and is re-visited in discussion. The second mechanism of strengthening, as well as the source of the stochastic variation in flow stress and the small-strain strain-hardening response, was revealed when the total dislocation source density was maintained as high as that in the real crystals, thus allowing dislocations to interact.

As mentioned previously, the initial FR source distribution produced a population of single-armed dislocations sources which repeatedly operated in the smaller samples (<10 μm) carrying out the straining. The contribution of such sources to flow stress varied for each specific simulation and cell size. These single-armed sources began to form at the statistically-determined source-truncation stress and persisted throughout the simulation regardless of the strain. The sources operated in the presence of other forest dislocation debris; thus at all times during the simulation a high dislocation density existed Consequently, the conditions for "dislocation starvation" as explicitly described in other studies were not observed [5, 9-14, 16].

Examination of the dislocation configurations at different time intervals for these simulations provided insights into the exhaustion-hardening response. The response is illustrated using two different examples of 1 μm tetragonal-cell simulations. In Fig. 5, 8 different snapshots of the dislocation configurations observed in a 1 μm simulation are depicted, along with the corresponding stress-strain curve. The starting dislocation source density is $2 \times 10^{12}/m^2$. The mobile-dislocation exhaustion processes involved in this sequence are junction formation and dipole interactions. Because of the limited number of mobile dislocation sources and high values of the stresses required to activate sources at the 1 μm size, "regular" forest-hardening processes, like junction formation and dipole interactions, result in the shutting off of scarcely-available dislocation sources and activation of less-weak sources at larger increments of stress. In larger cells, the number of available dislocation sources is larger and the strength of the sources is weaker because of correlated motion of segments linking interacting dislocations. These longer mobile segments make the exhaustion-hardening processes less effective.

As another example of exhaustion micromechanisms, Fig. 6, shows 8 different snapshots of the dislocation configurations observed in another 1 μm tetragonal-cell simulation, along with the corresponding stress-strain curve. Again, the starting dislocation source density is $2 \times 10^{12}/m^2$. The exhaustion processes involved in this sequence are junction, debris and pile-up formation. Again, the paucity of mobile dislocation sources leads to an example of activation of dislocation sources on slip systems with low Schmidt factors, 0.22 and 0.25. Also, debris and pile-up formation result in the exhaustion of dislocation sources.

After an exhaustion-hardening event, plastic deformation only continued when an increment of stress either freed the recently-pinned dislocation arm, or activated some other dislocation segment elsewhere in the simulation volume. However, in the 1 μm simulation cells, both the probability for having single-arm dislocation sources and the

maximum length for such sources are largely diminished—the statistical occurrences are biased by the free surfaces at small sizes [15]. This deficiency results in larger increases in stress to reactivate plastic flow, simply because of the finite number of available sources. In the simulations, eventually uninterrupted plastic flow occurred if the newly activated source could traverse the glide plane without the formation of new junctions, debris, etc. or, if the reactivated segment could traverse the glide plane by overcoming any newly-formed debris at the now-larger applied stress. Note that the absence of inertial and dynamic effects likely does not affect these findings. Even at the large stresses and strain rates intrinsic to these types of simulations, the maximum velocity of dislocation nodes only reached ~100 m/s, a value which is an order of magnitude lower than the limiting velocity of dislocations in Ni (~2000 m/s).

The simulated stress-strain curves for the larger 4 and 10 μm cells also reveal both truncation and exhaustion hardening; however, the overall hardening rates for exhaustion are much lower than those for the 1 μm simulation cells. In the larger cells, smaller incremental stress increases are sufficient to activate other existing primary–slip sources, as these volumes contain at least an order of magnitude more sources as compared to the 1 μm cells. In addition, secondary-slip systems are activated less frequently in the 4 and 10 μm simulation cells than in the 1 μm cells because of the lower overall stresses attained during straining. Finally, for the 4 and 10 μm cases, the first significant plastic-strain increment occurs at lower stresses since the probability of finding weaker long sources after source truncation is greater at larger sizes.

DISLOCATION DENSITY and STRAIN-RATE EFFECTS

Source Densities of 7 x 10^{11}/m^2 and 1 x 10^{13}/m^2

The effect of initial dislocation source density in the sample was examined. Figure 7 shows simulation results for the critical stress for three different initial dislocation source densities in the micrometer sized simulation cells, 7 x 10^{11}/m^2, 2 x 10^{12}/m^2 and 10^{13}/m^2, on a log-log plot (the 20 μm simulation results at an initial dislocation source density of 7 x 10^{11}/m^2 and 2 x 10^{12}/m^2 have been corrected for strain rate effects as described later). The strength-scaling exponent varies from approximately -0.84 at the low initial dislocation source density (7 x 10^{11}/m^2) to -0.43 at the high initial dislocation source density (10^{13}/m^2).

There are several sources of error in the determination of strength-scaling exponent from the simulation results: a) Selection of 'size' of the specimen as the length of the face diagonal of the tetragonal simulation cells. Another definition of size is the length of one of the sides of the cross-section, which is a factor of 1.414 smaller than the face diagonal. For such a case, the strength scaling exponent, *m,* has the same magnitude; however, the multiplying constant *K* in the equation $\tau = KD^{-m}$ decreases by a factor of $(\sqrt{2})^m$. b) The fluctuations in the critical stress at small sample sizes (1 μm) from one instantiation to another. The possible error in the determination of *m* due to the fluctuations is illustrated by considering an initial dislocation source density of 2 x 10^{12}/m^2. The standard error in the determination of the mean from 9 different samples is simply $\sigma/\sqrt{9}$ where σ is the standard deviation of the critical stress distribution at 1 μm. A log-log plot of the critical-

stress values at a dislocation source density of 2 x $10^{12}/m^2$ (similar to Fig. 4), where the 1 μm simulation-cell values are taken as $\pm$ *std.error* from their actual values, would show that the possible error in the determination of the scaling exponent due to fluctuations in the critical-stress is $m = 0.62 \pm 0.05$. This suggests that the variation in the scaling exponent at the three different initial dislocation source densities shown in Fig. 7 are well beyond the statistical error in the determination of *m* at each of these source densities. c) An uncertainty of $\pm 20\%$ in the critical-stress values from the selection of the simulation parameters, seg_{max}, seg_{min} (maximum and minimum segment lengths), r_{max} (maximum movement of a node per iteration) and r_{ann} (maximum collision distance between nodes). The possible effect on *m* due to this uncertainty was evaluated at an initial dislocation density of 2 x $10^{12}/m^2$, by changing the 1 μm critical-stress values from their measured ones by $\pm 20\%$. A log-log plot of the critical stress values resulting by altering the 1 μm-cell values, as indicated before, shows that *m* is 0.62 ± 0.09 due to this error. This once again suggests that the variation in the scaling exponent at the three different initial dislocation source densities shown in Fig. 8 are well beyond the statistical error in the determination of *m* at each of these source densities.

Strain Rate Effect in 20 μm Simulations

Figure 8 gives stress-strain-curve results from strain-rate change tests performed for a 20 μm cubic simulation cell, at two different initial dislocation source densities, 7 x $10^{11}/m^2$ and 2 x $10^{12}/m^2$. Results from simulations performed at a strain rate of 50/s are compared with results obtained from simulations where the strain rate was changed from 50/s at a certain portion in the elastic regime and deformed further at a strain rate of 10/s. The simulated stress-strain curves gradually transit from the elastic regime to a completely plastic regime with little or no strain hardening.

4 DISCUSSION

The opening of this manuscript described four characteristic size-affected flow features (i.e. power law strengthening with decreasing sample size, stochastic strength variation, intermittent flow and exhaustion hardening) associated with microcrystal compression testing. The present section discusses the dislocation micromechanisms observed via simulation that are qualitatively sufficient for explaining these experimentally-observed mesoscopic effects within an athermal limit. Critical to this are details gleaned from simulation about the dislocation-ensemble aspects of dislocation motion in small volumes of material. Some limitations of this and prior studies are also discussed together with selected suggestions for further study.

CELL SIZE DEPENDENT DISLOCATION MICROMECHANISMS

Elastic-Plastic Transition, Single-Arm Sources, and Truncation-Hardening

Though they range to simulation cell sizes of ~20 μm, the essential dislocation micromechanisms that lead to mesoscopic size effects were principally identified through the 1 μm cell simulations described here and, the single-source simulations described

elsewhere [19]. For the simulations containing FR sources of length greater than ~1/3 the slip-plane characteristic dimension, FR sources expand and intersect the surfaces of the cell, resulting in breaking the loops into two segments per source. The truncation first occurs at the elastic-plastic transition or 'zero-strain' level. The geometry of this hardening mechanism is qualitatively similar to that observed by Blanckenhagen, et. al., for constrained volumes [37, 39] but now alters stresses without a back stress or constraint.

After this, the system is temporarily dormant until there is a sufficient rise in applied stress to operate either of the two arms of any FR source in the volume as a spiral source. In selected instances and especially for the smallest sample sizes, this may occur on non-primary slip systems since the crystal has been hardened by truncation and stresses may have risen substantially. *Thus, the system seeks the weakest link in the newly formed population of single-arm sources*. At a critical stress and provided that no strong dislocation interactions take place, deformation proceeds via small repeated bursts at a constant stress level driven by single-arm sources repeatedly expanding and interacting with the free surfaces. The variation in critical stress depends solely upon the locations of source pins relative to the free surfaces, being independent of the initial FR source length. This critical aspect of the source stress in small volumes has received only preliminary investigation. Conceivably, for FR sources of much smaller sizes than the simulation cell (<< ~1/3 the cell dimension), an initial FR source could control flow. However, the probability of such sources controlling plastic deformation in weakest-link controlled real crystals decreases rapidly with sample size [15].

Motivated by the study of Parthasarathy, et. al. [15], Fig. 9 shows a histogram of the largest effective single-ended source lengths activated for 26 different instantiations of 1 μm tetragonal cells, each having an initial dislocation density of $2 \times 10^{12}/m^2$ (12 random FR sources per instantiation). For each instantiation, the length of the mobile FR sources (belonging to $(\bar{1}\bar{1}1)[110]$, $(\bar{1}\bar{1}1)[0\bar{1}1]$ and $(\bar{1}\bar{1}1)[\bar{1}10]$ slip systems) and the corresponding two single-ended source lengths for each FR source, was determined. The largest effective length among all the mobile sources was taken to control the initial plastic deformation and these are plotted in Fig. 9. The average of the length distribution is ~0.42 R and the standard deviation, ~0.15 R, where 'R' is $0.5a_o/\sqrt{2}$.

Hence, there is a progressively more probable involvement of the source characteristics that are set by the dislocation forest as the deforming volume increases for a given dislocation density but, the truncation of near-surface sources continues with a diminishing influence on τ^* at larger sizes. Since in the lower bound, single-arm sources operate at substantially lower stresses than FR sources of comparable length [19], only in the rarest of instances will some other smaller FR source set τ^*, until such point that the characteristic dimension of the sample approaches some ξ^* at a given dislocation density. Toward an upper bound, the strength of single-arm sources approaches that of FR sources, thus still controlling the stress. For the remainder of the manuscript, we refer to the statistical process of source-truncation hardening as the τ_{st} component of flow stress.

Altered Forest-Hardening Processes—Exhaustion Hardening

After attaining the source-truncation stress, the simulations also showed exhaustion hardening. That interval is dominated by 3d dislocation mechanisms that are understood

to be common to athermal forest hardening; i.e. junction and debris/source formation and dipole interactions. However, because of the limiting cell size (volume), such processes occurred for a dislocation forest that is statistically altered from that of macro-scale materials, thus containing an altered population of weakest-links. One may envisage that the altered statistical processes occur not only by the truncation and under-sampling of the ensemble of weakest-links relative to samples larger than some ξ^* but, also because of the synergistic effect of rising stresses from source hardening and the exhaustion itself. There may also be an enhanced localization of slip to fewer slip traces because of wide gaps in the spectrum of stresses required to spread slip after active slip-trace hardening occurs.

The simulations and experiments show that by comparison to the Stage II strain-hardening rate of macroscale FCC crystals, nominal exhaustion-hardening rates can be an order-of-magnitude greater. This occurs even though nothing within the simulations (beyond the source truncation at near-zero strain) is suggestive of qualitatively new micromechanistic processes. Rather, *exhaustion-hardening occurs by dislocation segment trapping and defeat mechanisms that are common to forest hardening, but by altered statistics of occurrence relative to macroscopic crystals*. For the remainder of the manuscript, we refer to the exhaustion-hardening component of the flow stress as, τ_{ex}, even though a quantitative definition for it cannot yet be provided.

The current results present a very different concept for dislocation sources and the stress-controlling dislocation configurations in microcrystals than that presented in the "starvation" model [11, 12, 16]. In these simulations only a very few mobile segments are needed to achieve substantial strains, provided that stresses permit those segments to exceed the glide resistance imposed by truncation and the dynamic dislocation structure. These processes may equivalently be called a "starvation" mechanism since the effect on τ^* is brought about by a deficiency in *mobile* density, ρ_m, as the system attempts to satisfy the kinetic equation ($\dot{\gamma} = \rho_m b v$) for samples smaller than ξ^*. However, in as much as mechanistic processes do not involve substantial reductions in the *total* dislocation density, ρ_t, and are controlled by the micromechanisms of forest-hardening, they are fundamentally different than the starvation mechanism envisaged by others [9, 11, 12, 14, 16]. Indeed, overall total dislocation densities progressively increase for all cell sizes with strain via the present micromechanisms, even with the intermittent presence of mobile-density-starved states [40, 42].

Intermittency and the Flow Stress Variation

Given the potent truncation- and exhaustion-hardening mechanisms, one might justifiably question what sets the break-away τ^* at differing values observed in simulation and experiment. That is, why do the simulation cells not display continued exhaustion hardening to the levels of the ideal material strength, especially for load-controlled testing? Within the single-slip areal-glide model [36], any dislocation forest will exhibit a 2d ξ which relates to a dislocation percolation threshold or percolation stress, τ^*. For a statistical distribution of variable-strength dislocation obstacles or obstacle clusters on a plane, obstacles are progressively defeated with rising stress and even the strongest obstacle or cluster in the plane will be defeated by cutting or looping once the percolation stress is reached. That is, the critical stress is provided by correlated

motion of mobile dislocation segments in that plane having an effective free-arm, λ_{eff}, (source) length that is equal-to-or-greater-than ξ ($\lambda_{eff} \geq \xi$). Thus, for large samples and high dislocation densities (large populations of sources), λ_{eff} hovers near ξ ($\lambda_{eff} \approx \xi$) on a slip-plane-by-plane basis, ρ_m exhibits a high stress sensitivity, τ^* exhibits a bulk-like response and, the mean-field forest law holds. For this condition flow tends to be smooth because of the high stress sensitivity of ρ_m on average, even though a local examination at the dislocation level would reveal intermittency. However, as the sample size or dislocation density decrease, the stress sensitivity of ρ_m decreases because of the dimensions limiting the distribution of sources vary, thus permitting a progressive separation between λ_{eff} and ξ (λ_{eff} being smaller than ξ) and eliciting a hardening response and intermittency to flow as the system attempts to maintain the required ρ_m.

These 2d micromechanistic processes are conceptually extensible into a 3d volumetric-glide model and they provide a conceptual definition of ξ^*. However, for 3d Stage I glide (more generally the "pre-plastic regime"), weakest-link slip-plane statistics on parallel slip planes will be important and there is no clear definition of a correlation length for slip plane spacing. Nonetheless, the concepts and results are qualitatively consistent with dislocation plasticity being a self-organized critical, depinning phase transition for commonly observed strain-rate regimes, as described elsewhere [45-55].

FLOW-STRESS SCALING RELATIONSHIPS

Figures 3a and 3b compare the stress-strain curves obtained from DDS with those from experiments on a common scale. The simulations qualitatively reproduce significant features of the experimental stress-strain curves for microcrystals of Ni including: significant increases in flow stress with decreasing sample size, a transition exhaustion-hardening regime, increasing scatter in the flow stress at smaller sizes and flow intermittency. However, there are important quantitative differences between the simulations. For example, the strain ranges over which the high size-affected stresses are achieved exhibit a variation from experiment [3, 5, 6, 8]. That is, larger strains are required for real crystals to achieve high critical stresses via source-truncation and exhaustion hardening than for the present simulations. This may be attributed to the assumption of a uniform stress distribution over the volume of the simulation cell in the calculations as well as other factors. Also, in real compression testing, end effects from misalignment of loading platen and the specimen and the effects from a compliant base, are expected to lead to a much shallower increase of the stress-strain curve in the pre-yielding region [56]. Finally, cross-slip, being a stochastic recovery and multiplication mechanism, may extend the strain range needed to achieve a given stress and raise the lower bound flow stress by enhancing obstacle formation. Ideally, the initial dislocation configuration used in the simulations needs to be cut out from an introduced network that is heavily jogged and the simulations need to consider cross-slip of both screw-oriented segments and at free surfaces for the production of dislocation sources. However, reliable procedures for introducing cross-slip and atomic-scale surface effects into 3d DDS are not established. Therefore, the present simulations only considered athermal mechanisms and qualitative effects.

From the simulation mechanistic results described previously, a discussion of the scaling relationship between τ^* and simulation cell size must consider three aspects. First, there is a scaling of the strength of individual dislocation sources near surfaces with their length. This size-scaling has been treated in detail elsewhere [19] and, was shown to lead to the relation

$$\tau_{source} \propto \ln(L)/L \qquad 1$$

However, that scaling relationship (following Parthasarthy, et. al. [15]) does not give the closely-related but statistically-modified scaling of τ_{st} defined by

$$\tau_{st} = k\mu \frac{\ln(\beta(R/b))}{\beta(R/b)} \qquad 2$$

having a standard deviation in τ_{st} dependent upon a parameter ΓR. Here, R is the radius of the specimen and β and Γ are multiplying constants lying between the values of 0 and 1 and, are functions of the number of mobile sources in the sample. Thus, the definition of τ_{st} provides the second important scaling relationship between τ^* and simulation cell size. For the smallest cells, the τ_{st} contribution dominates and may effectively be τ^*, depending upon the dislocation density. At larger cell sizes, as defined τ_{st} contributes a zero-strain source-hardening component to the reference stress. Note that neither of these relationships precisely indicates the $1/D$ scaling of τ^* predicted by others, nor do they yield a $D^{-0.5}$ relationship. Most notable from these two contributions to τ^* is that even though single-armed sources are weaker than FR sources at a given length, reasonable evaluations of the statistics of their occurrence in small samples suggest a strengthening effect. Those same reasonable statistics indicate that source-hardening alone is insufficient to describe τ^* in general [41, 42].

Figure 7 and Eqn. 3 describe the third level, τ^* scaling with sample size as

$$\tau^* \propto D^{-\kappa} \qquad 3$$

where κ is an exponent for which the magnitude varies with dislocation source density and D is the sample diameter. One may now expect that τ^* in Eqn. 3 consists itself of three parts: i) a *size independent* dislocation density contribution, τ_f; ii) an exhaustion hardening contribution that awaits quantitative definition, τ_{ex}; and iii) a source hardening contribution as described by Eqn. 2, τ_{st}. From the results and discussion presented here, it should be clear that a *single value for κ cannot be derived* for the 3d stochastic micromechanistic processes identified via simulation. As such, deformation of microcrystals that contain dislocation sources but are smaller than some ξ^* is fundamentally different and leads to different scaling relationships than those found for dislocation-free whiskers. Note that whisker-like effects were recently observed for microcrystals that are arguably dislocation free at the outset [57].

Nonetheless, a pragmatic evaluation including the simulation data, experimental results, specified dislocation densities, and appropriate normalization parameters leads to

the plot in Fig. 4. That figure shows that a wide set of small-free-volume deformation experiments and, the present simulations, appear to be well-described by a power-law relationship between τ^* and a characteristic dimension, with wide scatter. Encouragingly, the 3d DDS simulation results are in good agreement with the microcrystal test results for pure Ni, Au, Cu and Al, even though only athermal mechanisms were included. Here, the value of κ ranges from ~-0.4 to ~-0.84, depending primarily upon the initial dislocation source density, for samples larger than ~1 μm and densities on-the-order of $10^{11} - 10^{14}/m^2$. Interestingly, the characteristic length of ~1 μm relates well to the 'rule-of-thumb' obtained from the forest-hardening model indicating that the strongest, τ^*-controlling obstacles to glide, have a characteristic spacing given by $\lambda_c = 1/\sqrt{\rho_o/10}$ in single slip. The value of κ also agrees with that found by Yu and Spaepen where stress-scaling exponents of -0.58 to -0.82 were deduced from tests of polycrystalline Cu thin films [58]. Thus, the scaling of results shown in Fig. 4, taken together with the simulated stress-strain curves and analysis of the simulation results, strongly suggest a *qualitative sufficiency* to micromechanisms controlling the size-affected τ^* for samples ranging between a lower limit of λ_c and an upper limit set by ξ^* for macroscopic samples.

IMPLICATIONS TO PRIOR WORK

As defined herein, the size-dependent scaling of τ^* is a result of three strengthening mechanisms present in micrometer-sized simulation cells: i) source-truncation hardening, ii) exhaustion hardening and iii) forest hardening. Of these, the exhaustion hardening is indicative of the existence of ξ^* in a vein similar to that described Gil Sevillano, et. al. [36], and is clearly tied to volumetric influences just as are dislocation-forest processes. The simulations also suggest an important strengthening mechanism which is surface dominated, source truncation and, support a model for this given previously [15]. Taken together these mechanisms are consistent with prior phenomenological arguments [59, 60], in that a surface-like effect becomes important for small simulation cells. The source-truncation mechanism is expected to have a decreasing contribution to τ^* with increasing dislocation density at small crystal sizes, since the probability of finding weak dislocation sources increases with increasing dislocation density (see Eqn. 2, increasing β). At large crystal sizes the surface effects are diminished and, are almost independent of initial dislocation source density. The exhaustion-hardening mechanism depends upon the initial mobile dislocation density, as well as the initial forest density. Therefore, its dependence on dislocation density is complicated at small specimen sizes. At large specimen sizes it is expected to be minimal and independent of initial dislocation density. The third mechanism, forest hardening, which is defined here as being independent of crystal size, increases with increasing dislocation density. As a result of these mechanisms, the flow-stress-scaling exponent decreases from one that is indicative of surface-like behavior at low dislocation densities (approximately -1), to one that is indicative of bulk-like behavior at high densities. It is noted that if the initial dislocation density is made much larger ($\sim 10^{15}/m^2$), one might expect that forest hardening would dominate the flow behavior and the critical stress would be independent of crystal size in the micrometer-size range. Finally, note that these hardening effects are fundamentally

different than nucleation-controlled size-effects since the samples plastically harden to the flow stress.

There have been other treatments of surface effects on flow stress using 2d DDS methods [9, 13, 14, 61]. However, unlike those prior treatments the present 2d source-truncation mechanism occurs in the glide plane of the dislocation, not in the plane normal to the dislocations. Also, to properly account for its magnitude one must consider dislocation ensembles in 3d. The present exhaustion processes occur over a wide range of source strengths for relatively small changes to the dislocation density; whereas, the selected geometry of effectively infinitely long parallel dislocation lines of prior 2d simulations, leads to an accumulation of internal stresses via dislocation storage (pile-up stresses) that are envisaged as necessary to soften samples having only a narrow range of source-activation stresses. Conversely, for the present 3d simulations, dislocation pile-ups were shown to harden active sources, consistent with forest-hardening theory. Further, by the nature of the 2d "end-on infinite lines" model that has frequently be employed, one maximizes the influence of image forces on the dislocations in a manner that may be unrealistic for the 3d nature of dislocation glide in real materials and as supported by the present and other simulations [62, 63]. Thus, it is not surprising that the prior 2d DDS treatments result in stress-strain curves that are markedly different than those known from microcrystal experiments, particularly in the post-yielding regime [9, 10, 13, 14, 61, 64].

UNRESOLVED ISSUES and NEEDED FUTURE WORK

The 3d DDS studies reported here leave a number of open or unresolved issues to consider for future studies. For example, there are no studies of the effects of the nature of dislocation sources beyond those which included FR sources as a part of the initial conditions. These should be expanded to include various surface-source configurations, with and without internal dislocation pins in order to more fully understand the starvation-hardening mechanisms argued to occur for smaller specimen sizes. The studies are important for resolving the question of what τ^* scaling law should occur for samples that are smaller than the characteristic strong-obstacle dimension, λ_c, of the dislocation forest as discussed previously. The phenomenological aspects of the flow curves that are reported for such cases seem to suggest that the microcrystals are able to form an ample dislocation density but its origins are unclear.

As was mentioned, there has not been a study of the role of cross-slip that adequately addresses dislocation ensembles. Note that Fig. 3a shows a near zero strain-hardening rate for the 10 and 20 μm samples which we believe is an athermal artifact. Prior studies suggested that cross-slip is unimportant for simulation cells below ~1 μm; however, the differences between the simulated stress-strain curves and those from experiment may suggest otherwise [17, 18, 37-39]. The absence of a Stage I strain-hardening response of the large simulations, and the presence of an extended strain range for developing the flow stress in experimental microcrystals, both suggest an incomplete treatment of multiplication and recovery processes—both of which are dominated by cross-slip in macroscopic crystals. These processes may also be important for bringing about the appropriate scale-free flow response under the loading conservation law for selected tests as discussed elsewhere [51, 55, 65]. Further, the existence of single arm sources within

the simulation cells suggests that there is no fundamental limit (short of complete shearing of the sample) on the life-time or total strain that a source can contribute, thus there may be no practical "breeding length" limitations as were suggested by prior studies [5]. That result may also be incompatible with a recent report by Csikor, et. al. [55].

Finally, we note that the mechanisms identified here must be further considered for the deformation geometries associated for deformation of thin films and for nanoindentation. Both of those frequently include both dislocation sources limited by free surfaces and a dislocation forest constrained in its physical dimension ($\lambda_{eff} < \xi^*$).

5 SUMMARY & CONCLUSIONS

A 3d DDS method was used to examine athermal size-dependent strengthening in microcompression for simulation cells smaller than an estimated correlation length, ξ, established by the initial dislocation density. The results of numerous simulations containing free-surface boundary conditions and initial dislocation densities of 7×10^{11} to $10^{13}/m^2$, were analyzed for simulation cells having a characteristic dimension ranging from 0.5-20 μm. The simulations were analyzed to identify the evolution of dislocation sources in the presence of free surfaces and the micromechanisms of dislocation interactions in small volumes. Those micromechanisms were evaluated within the context of the forest hardening theory and selected other studies of size-affected plasticity. The following conclusions are drawn from the study:

1. Two important size-dependent mechanisms of stress increase at small sizes were found to exist beyond mean-field forest hardening. First, dislocation source truncation by free surfaces sets a characteristic length, $<\lambda_{max}>$, and a size-dependent stress, τ_{st}. Second, 3d dislocation processes lead to exhaustion hardening, τ_{ex}, that is exacerbated at small physical dimensions that depend on dislocation density. Neither of these is unto itself is sufficient to explain the experimental findings, but when considered collectively in the presence of forest hardening, may explain the strengthening.

2. The small dimensions both change the stochastic population of strain carriers at a given stress and result in higher stresses that can enhance exhaustion-hardening. Those micomechanisitic processes are qualitatively equivalent to ordinary forest hardening. However, the exhaustion hardening leads to a different quantitative relationship between flow stress and dislocation density because of altered dislocation interaction statistics for dimensions limited below some ξ^*.

3. The athermal 3d DDS results also yield similar dimensional scaling of the flow stress to what is found in experiments on FCC microcrystals, with only the initial dislocation source density as an input. Further, the technique results in qualitatively similar stress-strain curves as those from experiment, again for an athermal treatment of the dislocation ensemble. Thus, the identified micromechanisms are viewed as being qualitatively sufficient for explaining the size-affected flow stress.

4. The simulations resulted in a size-dependent depinning transition at the flow stress, just as found for experiments. This transition could not be quantitatively compared with experiments because of differences in strain rate, relatively low strains and an absence of thermally-activated processes in the simulations.

5. The source-truncation mechanism operates at effectively zero strain, thus suggesting an important omission from common continuum plasticity models, including those for strain-gradient plasticity. Further, the exhaustion hardening mechanism is expected to operate whenever the dislocation structure evolves at dimensions below some ξ^*. Thus, it is important for strain-gradient based plasticity models to consider the scale of the strain gradients relative to the physical scale of the current ξ^*. Such effects may be important to understanding the depth-dependence of hardness and the flow-stress of thin-film and fine-grained materials.

Acknowledgement
The authors acknowledge use of the 3d dislocation dynamics code, ParaDiS, which was developed at Lawrence Livermore National Laboratory by Dr. Vasily Bulatov and co-workers. The work of M. Tang is performed under the auspices of the United States Department of Energy by the University of California under Contract No: W-7405-ENG-48. We also acknowledge Dr. R. LeSar of Los Alamos National Laboratory and Prof. Ed Nadgorny of Michigan Technological University for discussions throughout the effort.

References

1. Uchic MD, Dimiduk DM, Florando JN, Nix WD. Exploring specimen size effects in plastic peformation of $Ni_3(Al,Ta)$ In: E.P. George, H. Inui, M.J. Mills, G. Eggeler, editors. *Defect Properties and Related Phenomena in Intermetallic Alloys*, Materials Research Society Symposium Proceedings, vol. 753. Pittsburgh (PA): Materials Research Society 2003. p.27.
2. Uchic MD, Dimiduk DM, Florando J, Nix WD. Science 2004; 305: 986
3. Dimiduk DM, Uchic MD, Parthasarathy TA. Acta Mater. 2005; 53: 4065
4. Uchic MD, Dimiduk DM. Mater. Sci. Engr. A. 2005; 400–401: 268
5. Greer JR, Oliver WC, Nix WD. Acta Mater. 2005; 53: 1821
6. Volkert CA, Lilliodden E. Philos. Mag. 2006; 86: 5567
7. Kiener D, Motz C, Schoberl T, Jenko M, Dehm G. Adv. Engr. Mater. 2006; 8: 1119
8. Nadgorny E, Dimiduk DM, Uchic MD. Mater. Res. Soc. Symp. Proc. 2006; 976: EE06-24
9. Deshpande VS, Needleman A, Van der Giessen E. J Mech. Phys. Solids 2005; 53: 2661
10. Shaver NF, Benzerga AA. TiiMS, 2005; 1
11. Greer JR, Nix WD. Phys. Rev. B 2006; 73: 245410
12. Greer JR. Rev. Adv. Mater. Sci. 2006; 13: 59
13. Balint DS, Deshpande VS, Needleman A, Van der Giessen E. Modelling Simul. Mater. Sci. Eng. 2006; 14: 409
14. Benzerga AA, Shaver NF. Scripta Mater. 2006; 54: 1937

15. Parthasarathy TA, Rao SI, Dimiduk DM, Uchic MD, Trinkle DR. Scripta. Mater. 2007; 56: 313
16. Nix WD, Greer JR, Feng G, Lilleodden E. Thin Solid Films 2007; 515: 3152
17. Weygand D, Poignant M, Gumbsch P, Kraft O. Mater. Sci. Engr. A 2007; in press
18. Tang H, Schwarz KW, Espinosa HD. Acta Mater. 2007; 55: 1607
19. Rao SI, Dimiduk DM, Tang M, Parthasarathy TA, Uchic MD, Woodward C. Philos. Mag. 2007; 87: 4777
20. Dimiduk DM, Uchic MD, Rao SI, Woodward C, Parthasarathy TA. Modelling Simul. Mater. Sci. Engr. 2007; 15: 135
21. Devincre B, Kubin LP, Lemarch C, Madec R. Mater. Sci. Eng. A 2001; 309-310: 211
22. Tang M, Fivel M, Kubin LP. Mater. Sci. Eng. A 2001**;** 309-310: 256
23. Madec B, Devincre B, Kubin LP. Phys. Rev. Ltrs. 2002; 89: 255508
24. Bulatov V, Hsiung LL, Tang M. Nature 2006; 440: 1174
25. Zbib HM, Aifantis EC. Scripta Mater. 2003; 48: 155
26. Cai W, Bulatov V, Pierce T, Hiratani M, Rhee M, Bartelt M, Tang M. Massively-parallel dislocation dynamics simulations in Solid Mechanics and Its applications, edited by Kitagawa, H. & Shibutani, Y. (Kluwer Academic Publishers) 2004;115:1
27. Arsenlis A, Cai W, Tang M, Rhee M, Oppelstrup T, Hommes G, Pierce TG, Bulatov VV. Modelling Simul. Mater. Sci. Eng. 2007; in press
28. Gil Sevillano J. Flow Stress and Work Hardening in: H. Mughrabi editor *Plastic deformation and fracture of crystalline materials,* Materials Science and Technology 1989; 6: 21
29. Basinski SJ, Basinski ZS. in: F.R.N. Nabarro editor, *Dislocations in Solids* 1979;4: 261 (North Holland, Amsterdam)
30. Kocks UF, Mecking H. Prog. Mater. Sci. 2003; 48: 171
31. Nadgorny E. Prog. Mater. Sci. 1988; 31: 487
32. Berdichevsky V. J. Mech. Phys. Solids 2005; 53: 2457
33. Berdichevsky V, Dimiduk DM. Scripta Mater. 2005; 52: 1017
34. Kocks UF. *Dislocations and Properties of Real Materials*, 1985; p125 (The Institute of Metals, London)
35. Gil Sevillano J, Bouchaud E, Kubin LP. Scripta Mater. 1991; 25: 355
36. Gil Sevillano J, Ocaña Arizcorreta I, Kubin LP. Mat. Sci. Engr. A 2001; 309-310: 393
37. Von Blankenhagen B, E. Arzt E, Gumbsch P. Acta Mater. 2004; 52: 773
38. Von Blankenhagen B, Gumbsch P, Arzt E. Philos. Mag. Ltrs. 2003; 83: 1
39. Von Blankenhagen B, P. Gumbsch P, Arzt E. Modelling. Simul. Mater. Sci. Engr. 2001; 9: 157
40. Polasik S. M.S. Thesis, The Ohio State University 2005
41. Norfleet DM. Ph.D. Thesis, The Ohio State University, August 2007
42. Norfleet DM, Uchic MD, Mills MJ, Dimiduk DM. Acta Mater. 2007; submitted for publication
43. Neuhauser H. Dislocations in Solids, edited by F.R.N. Nabarro, 1983; 6: 321 (North-Holland, Amsterdam)
44. www.paraview.org
45. Miguel M-C, Vespignani A, Zapperi S, Weiss J, Grasso J-R. Nature 2001; 410: 667
46. Koslowski M, LeSar R. Thomson R. Phys. Rev. Lett. 2004; 93: 125502

47. Koslowski M, LeSar R. Thomson R. Phys. Rev. Lett. 2004; 93: 265503
48. Zaiser M, Moretti P. J. Stat. Mech. 2005; 10: 1088/1742-5468/2005/08/P08004
49. Miguel M-C, Moretti P, Zaiser M, Zapperi S. Mater. Sci. Eng. A 2005; 400-401: 191
50. Richeton T, Weiss J, Louchet F. Acta Mater. 2005; 53**:** 4463
51. Dimiduk DM, Woodward C, LeSar R, Uchic MD. Science 2006; 312: 1188
52. Zaiser M. Adv. Phys. 2006; 55: 185
53. Dimiduk DM, Woodward C, Uchic MD, Rao SI, Parthasarathy TA. Proc. 3rd Int. Conf. Multiscale Mater. Model. 2006;282 (Fraunhofer IRB Verlag, Freiburg, Germany)
54. Schwerdtfeger J, Nadgorny E, Madani-Grasser F, Koutsos V, Blackford JR, Zaiser M. J. Stat. Mech. 2007;10:1088/1742-5468/2007/04/L04001
55. Csikor FF, Motz C, Weygand D, Zaiser M, Zapperi S. Science 2007; 318: 251
56. Choi YS, Uchic MD, Parthasarathy TA, Dimiduk DM. Scripta Mater. 2007; 57: 849
57. Bei H, Shim S, George EP, Miller MK, Herbert EG, Pharr GM. Scripta Mater. 2007; 57: 397
58. Yu DYW, Spaepen F. J. Appl. Phys. 2003; 95: 2991
59. Carpinentri A, Pugno N. Nature Mater. 2005; 4: 421
60. Sieradzki K, Rinaldi A, Friesen C, Peralta P. Acta Mater. 2006; 54: 4533
61. Han CS, Hartmaier A, Gao H, Huang Y. Mater. Sci. Eng. A 2006; 415: 225
62. Hazzledine PM. in Fundamentals of Deformation and Fracture, edited by B.A. Bilby, et al., C.U.P. 1985; 385
63. Hartmaier A, Fivel MC, Canova GR, Gumbsch P. Modelling Simul. Mater. Sci. Eng. 1999; **7**: 781
64. Guruprasad PJ, Benzerga AA. J. Mech. Phys. Solids 2007; in press
65. Vespignani A, Zapperi S. Phys. Rev. E, 1998; 57: 6345
66. Verdier M, Fivel MC, Groma I. Modelling Simul. Mater. Sci. Eng. 1998; 6: 755
67. Weygand D, Friedman LH, Van der Giessen E, Needleman A. Modelling Simul. Mater. Sci. Eng. 2002; 10: 437
68. Bonneville J, Escaig B. Acta. Metallurgica 1979; 27: 1477

Figure Captions

Figure 1: A view of the dislocation microstructure at the proportional limit load for A) 1 μm, B) 4 μm, C) 10 μm and D) 20 μm simulation cells. Color scheme: In (A) and (B), $(\bar{1}\bar{1}1)[110]$, primary – green; $(\bar{1}\bar{1}1)[0\bar{1}1]$, secondary – yellow; $(1\bar{1}1)[\bar{1}10]$, secondary – orange; Rest – blue. In (C) and (D), $(\bar{1}\bar{1}1)[110]$, primary – green; Rest – blue .

Figure 2: a) Stress-strain curves obtained from 3d DDS for tetragonal 1 μm simulation cells of Ni ($\rho_o = 2 \times 10^{12}/m^2$) having an aspect ratio of 2.8. Also shown in b) are the stress-strain, dislocation density vs. time and plastic strain vs. time plots obtained for a single FR source in a 1 μm cubic cell. The stress-strain curves have been scaled to a shear modulus of 78.6 GPa, from a shear modulus of 59.9 GPa.

Figure 3: Comparison of stress-strain curves obtained in the size range 1 – 20 μm for a) simulations ($\rho_o = 2 \times 10^{12}/m^2$) and b) experiments on microcrystals of Ni. The simulated

stress-strain curves have been scaled to a shear modulus of 78.6 GPa, from a shear modulus of 59.9 GPa.

Figure 4: A comparison log-log plot of the critical resolved shear stress at 1% total strain, scaled by the shear modulus G, and normalized to the Burger's vector of Ni, b_{ni}, versus size of the Ni microcrystal, showing experimental (Ni and Au) and simulation (ρ_o = 7 x 10^{11}/m^2, 2 x 10^{12}/m^2, and 10^{13}/m^2) results.

Figure 5: A plot of eight different time-evolved dislocation configurations in a 1 μm tetragonal simulation cell, along with the corresponding stress-strain curve. The position on the stress-strain curve for the different dislocation configurations is marked. Color scheme: $(\bar{1}\bar{1}1)[110]$, primary – green; $(\bar{1}\bar{1}1)[0\bar{1}1]$, secondary – yellow; $(\bar{1}1\bar{1})[\bar{1}10]$, secondary – orange; rest – blue. A) Initial dislocation microstructure introduced into the simulation cell. B) Secondary $(\bar{1}1\bar{1})[\bar{1}10]$ FR source in the middle of the simulation cell interacts with the surface to form two single-ended sources and the longer of the two sources interacts with a primary $(\bar{1}\bar{1}1)[110]$ source to form a Hirth lock, $(10\bar{1})[010]$. C) Interaction of the second secondary source at the bottom of the simulation cell with a forest dislocation source $(111)[\,10\bar{1}]$ to form a glide lock $(111)\,[01\bar{1}]$. Operation of the third secondary source at the top of the simulation cell. D) The third secondary source forms two single ended sources from interaction with the surface and the longer of the two single-ended sources thus formed feels the back stress from the Hirth-lock configuration. E) The single-ended source overcomes the back stress from the Hirth-lock configuration and traverses its glide plane and feels a dipole like interaction from the other secondary source which is part of the Hirth lock. F) The single-ended source overcomes the dipole interaction. G) Hirth lock is defeated and reforms the original primary source, as well as the single-ended source from the second secondary source. Dipole interaction between this secondary and the traversing source locks the traversing source at this position. H) Dipole interaction is overcome and the third secondary source traverses freely on its glide plane. It activates the primary source close to it, resulting in the primary source traversing its glide plane. Glide lock formed between the secondary source at the bottom of the simulation cell and a forest dislocation source is overcome and the secondary source at the bottom of the simulation cell starts traversing its glide plane.

Figure 6: A plot of eight different time-evolved dislocation configurations in a 1 μm tetragonal simulation cell, along with the corresponding stress-strain curve. The position on the stress-strain curve for the different dislocation configurations is marked. Color scheme: $(\bar{1}\bar{1}1)[110]$, primary – green; $(\bar{1}\bar{1}1)[0\bar{1}1]$, secondary – yellow; $(\bar{1}1\bar{1})[\bar{1}10]$, secondary – orange; $(\bar{1}1\bar{1})[011]$, secondary – pink; $(111)[10\bar{1}]$, secondary – red; rest – blue. A) Initial dislocation microstructure in the simulation cell. B) Largest of the highly stressed sources belonging to the $(\bar{1}\bar{1}1)[0\bar{1}1]$ slip system operates, interacts with the

surfaces and forms two single-ended sources. C) A long source belonging to the $(111)[10\bar{1}]$ slip system operates, interacts with the surfaces and forms two single-ended sources. D) The longer of the two single-ended sources belonging to the $(\bar{1}\bar{1}1)[0\bar{1}1]$ slip system operates. E) Longer of the two single-ended sources belonging to the $(111)[10\bar{1}]$ slip system operates. F) Source belonging to the $(11\bar{1})[011]$ system operates. G) Operating $(11\bar{1})[011]$ source interacts with the operating $(111)[10\bar{1}]$ slip system source and forms a (001)[110] Lomer-Cottrell debris, which is sessile. H) Repeated operation of both the $(11\bar{1})[011]$ and $(111)[10\bar{1}]$ sources, leads to the formation of a pile-up on either side of the Lomer-Cottrell debris, leading to exhaustion of both these sources.

Figure 7: A log-log plot of the critical resolved shear stress at 1% total strain, scaled by the shear modulus *G*, versus size of the simulation cell, obtained in the 3d DDS studies for three different initial dislocation source densities, $7 \times 10^{11}/m^2$, $2 \times 10^{12}/m^2$ and $10^{13}/m^2$. A power law fit to the results at the three different initial dislocation source densities is also shown.

Figure 8: Stress-strain curves obtained from 3d DDS for a 20 μm cubic simulation cell at two different initial dislocation source densities, $7 \times 10^{11}/m^2$ and $2 \times 10^{12}/m^2$ and, at two different applied strain rates, 10 and 50/s. The stress-strain curves have been scaled to a shear modulus of 78.6 GPa, from a shear modulus of 59.9 GPa.

Figure 9: Histogram (number) of the estimated effective length of weakest sources for 26 different random instantiations of 1 μm tetragonal simulation cells. Each instantiation had 12 different random FR sources (random lengths, random slip system and random orientation). The initial plastic deformation of 5 out of the 26 different instantiations was controlled by the initial FR source lengths. In 23 of the 26 different cases, the primary slip plane $(\bar{1}\bar{1}1)$ was activated. In the other three, the secondary slip plane, $(11\bar{1})$ was activated.

Table 1: Number of simulations performed and number of initial Frank-Read sources introduced into the simulation cell (italicized) as a function of the simulation cell size and the initial dislocation source density.

	Dislocation source density, ρ_0		
Size (μm)	***$7x10^{11}/m^2$***	***$2x10^{12}/m^2$***	***$10^{13}/m^2$***
0.5	-	-	5-10, *12*
1	5-10, *4*	5-10, *12*	5-10, *48*
4	3, *64*	3, *192*	3, *768*
10 (tetragonal)	-	2, *1200*	-
10 (cubic)	2, *200*	2, *600*	2, *2400*
20 (cubic)	2, *800*	2, *2400*	-

Fig.1:

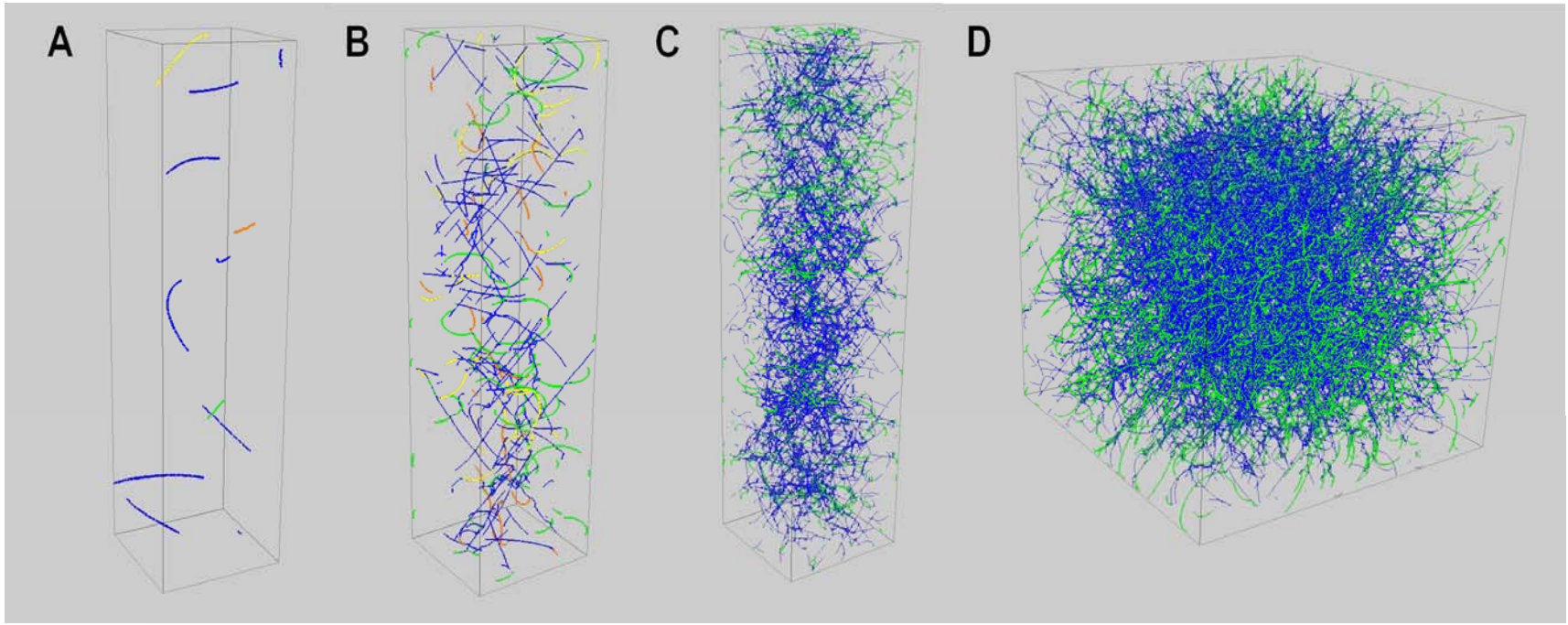

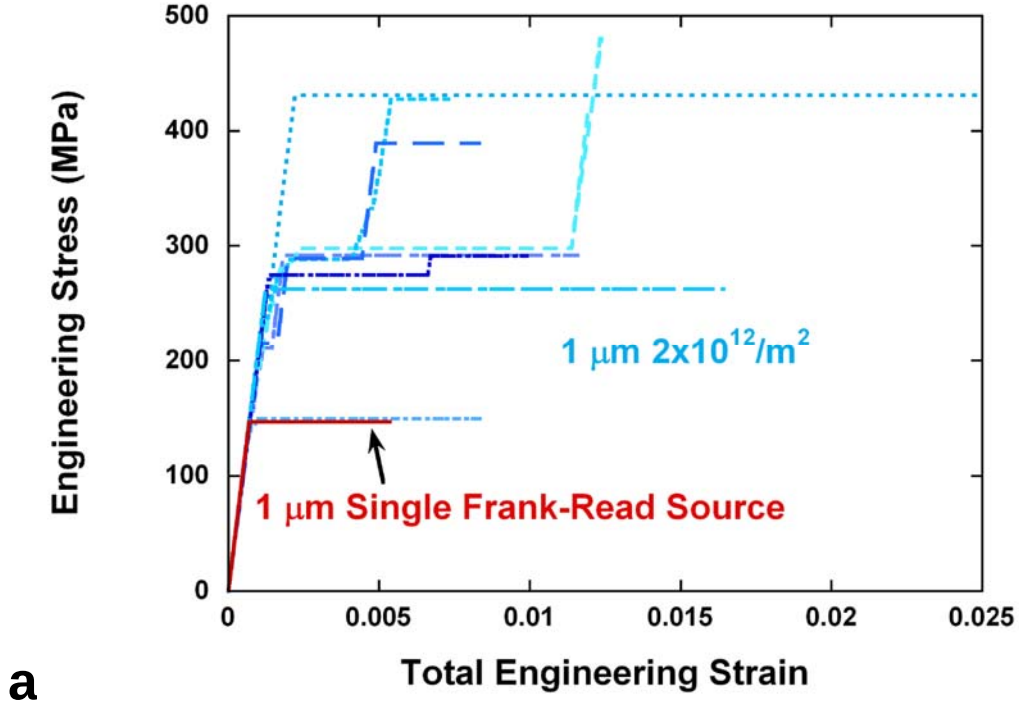
Engineering Stress (MPa)
500
400
300
200
100
0
0
0.005
0.01
0.015
0.02
0.025
Total Engineering Strain
1 μm 2x10^12/m^2
1 μm Single Frank-Read Source

a

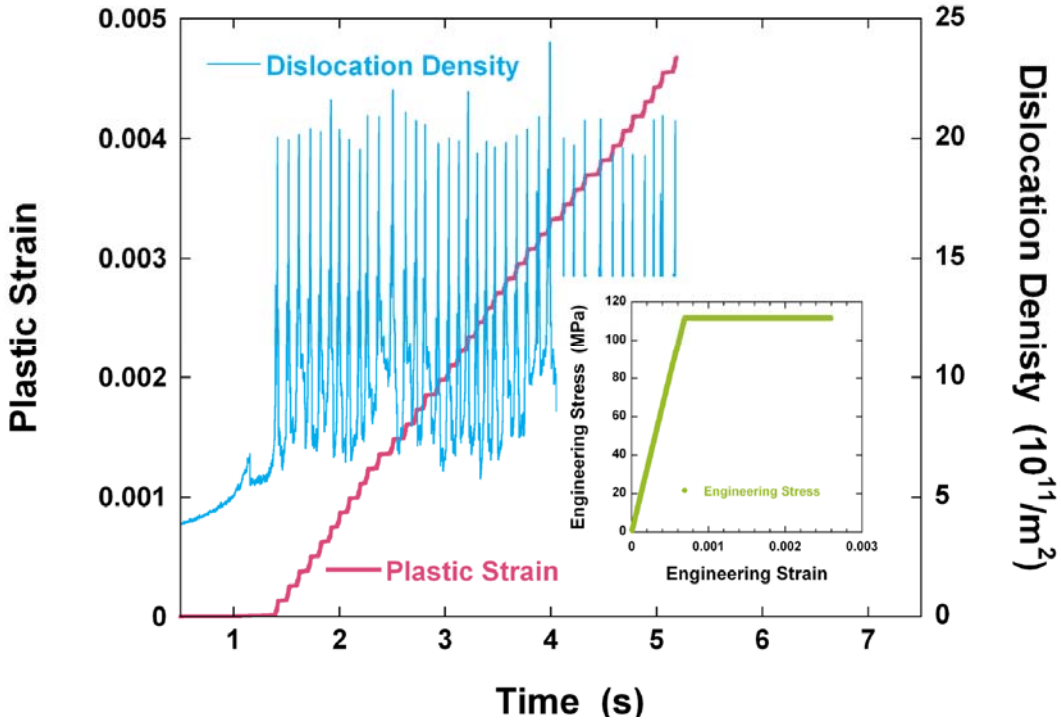
Plastic Strain
Dislocation Density (10^11/m^2)
Time (s)
Dislocation Density
Plastic Strain
Engineering Stress (MPa)
Engineering Strain
Engineering Stress

b

Fig.2

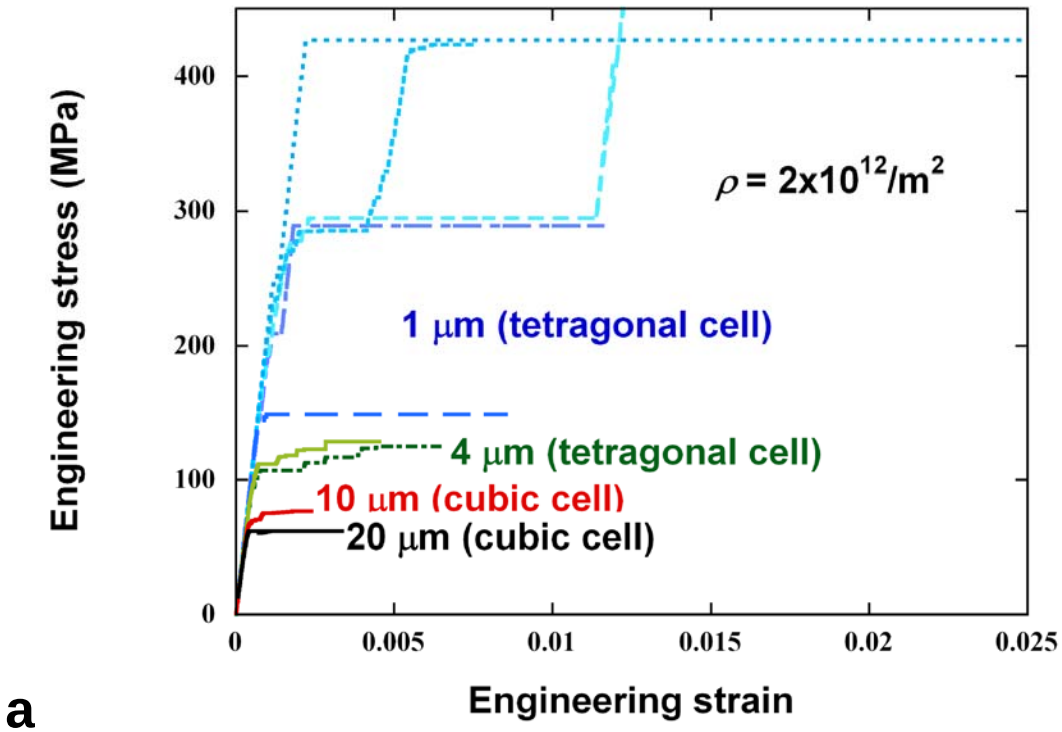
Engineering stress (MPa)
400
300
200
100
0
0
0.005
0.01
0.015
0.02
0.025
Engineering strain
$\rho = 2x10^{12}/m^2$
1 μm (tetragonal cell)
4 μm (tetragonal cell)
10 μm (cubic cell)
20 μm (cubic cell)

a

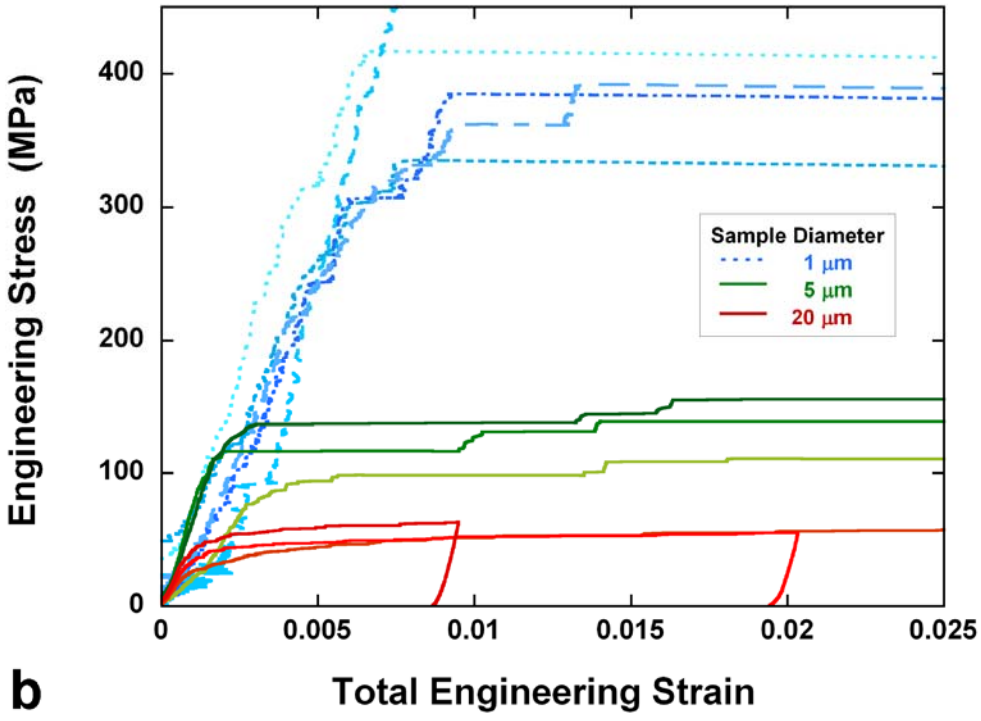
Engineering Stress (MPa)
400
300
200
100
0
0
0.005
0.01
0.015
0.02
0.025
Total Engineering Strain
Sample Diameter
1 μm
5 μm
20 μm

b

Fig 3:

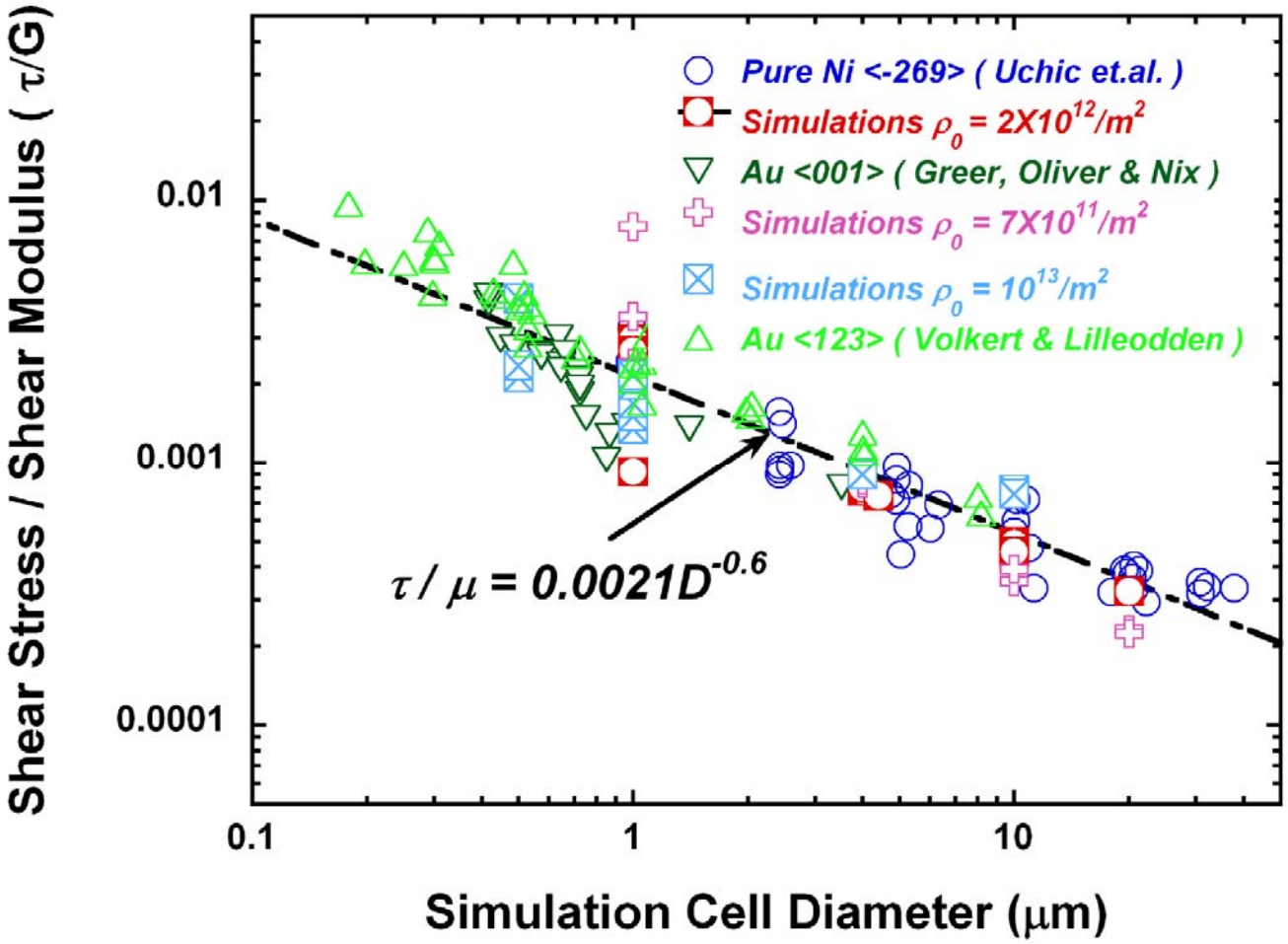
Shear Stress / Shear Modulus (τ/G)
0.01
0.001
0.0001
0.1
1
10
Simulation Cell Diameter (μm)
Pure Ni <-269> (Uchic et.al.)
Simulations ρ0 = 2X10^12/m^2
Au <001> (Greer, Oliver & Nix)
Simulations ρ0 = 7X10^11/m^2
Simulations ρ0 = 10^13/m^2
Au <123> (Volkert & Lilleodden)
τ / μ = 0.0021D^-0.6

Fig 4:

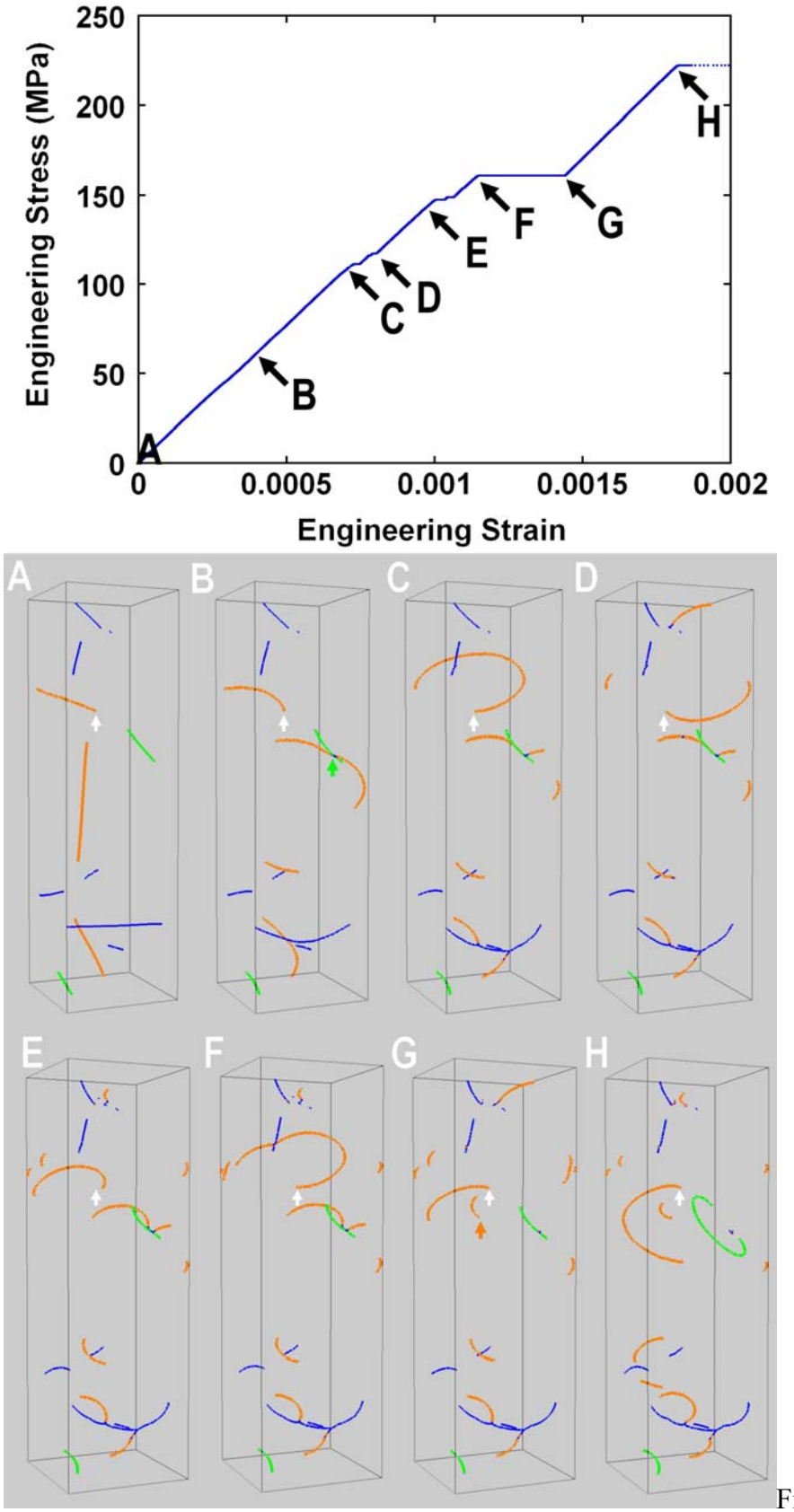
Engineering Stress (MPa)
250
200
150
100
50
0
0
0.0005
0.001
0.0015
0.002
Engineering Strain
A
B
C
D
E
F
G
H

Fig.5:

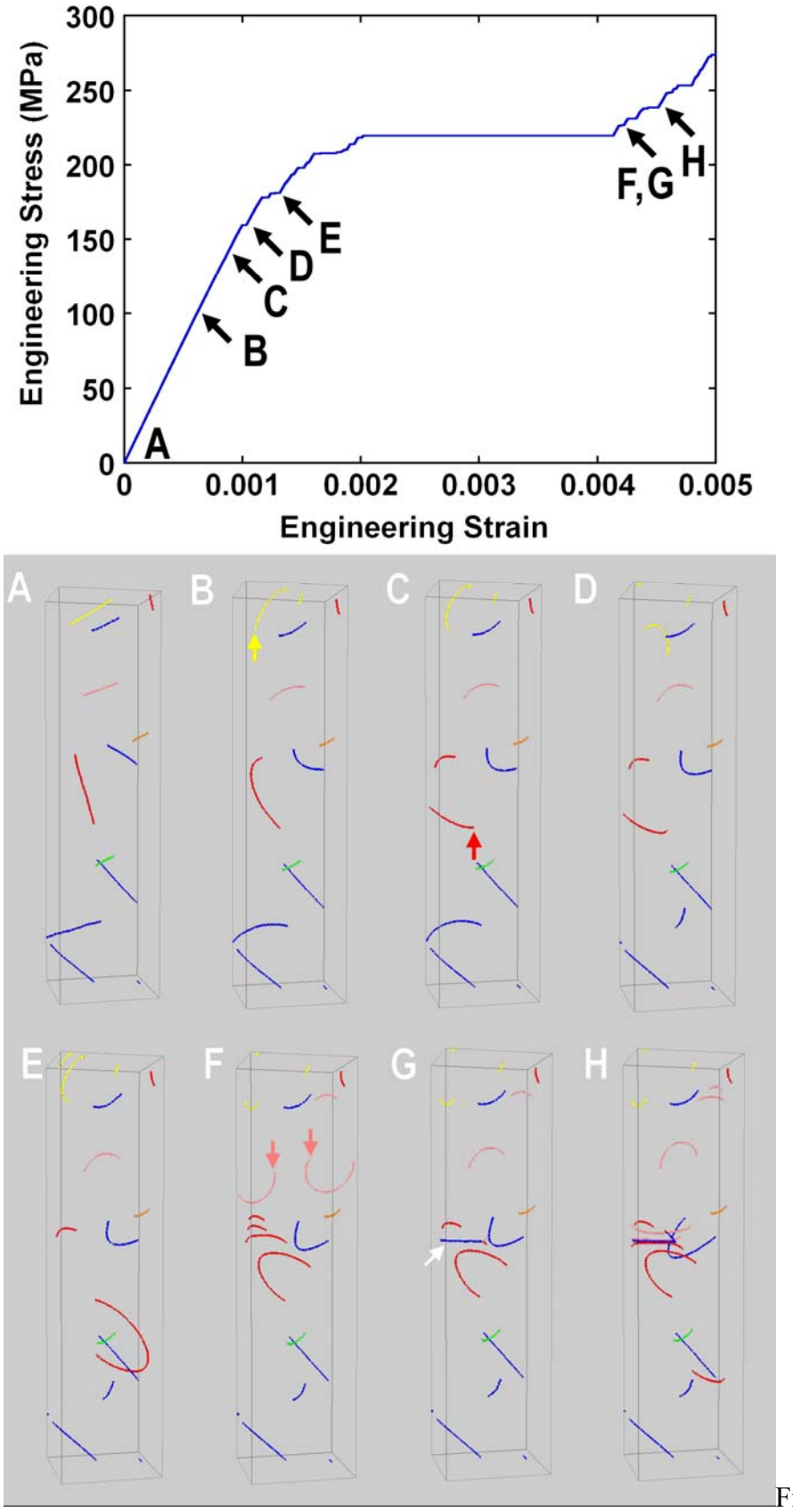
Engineering Stress (MPa)
300
250
200
150
100
50
0
0
0.001
0.002
0.003
0.004
0.005
Engineering Strain
A
B
C
D
E
F,G
H
A
B
C
D
E
F
G
H

Fig.6:

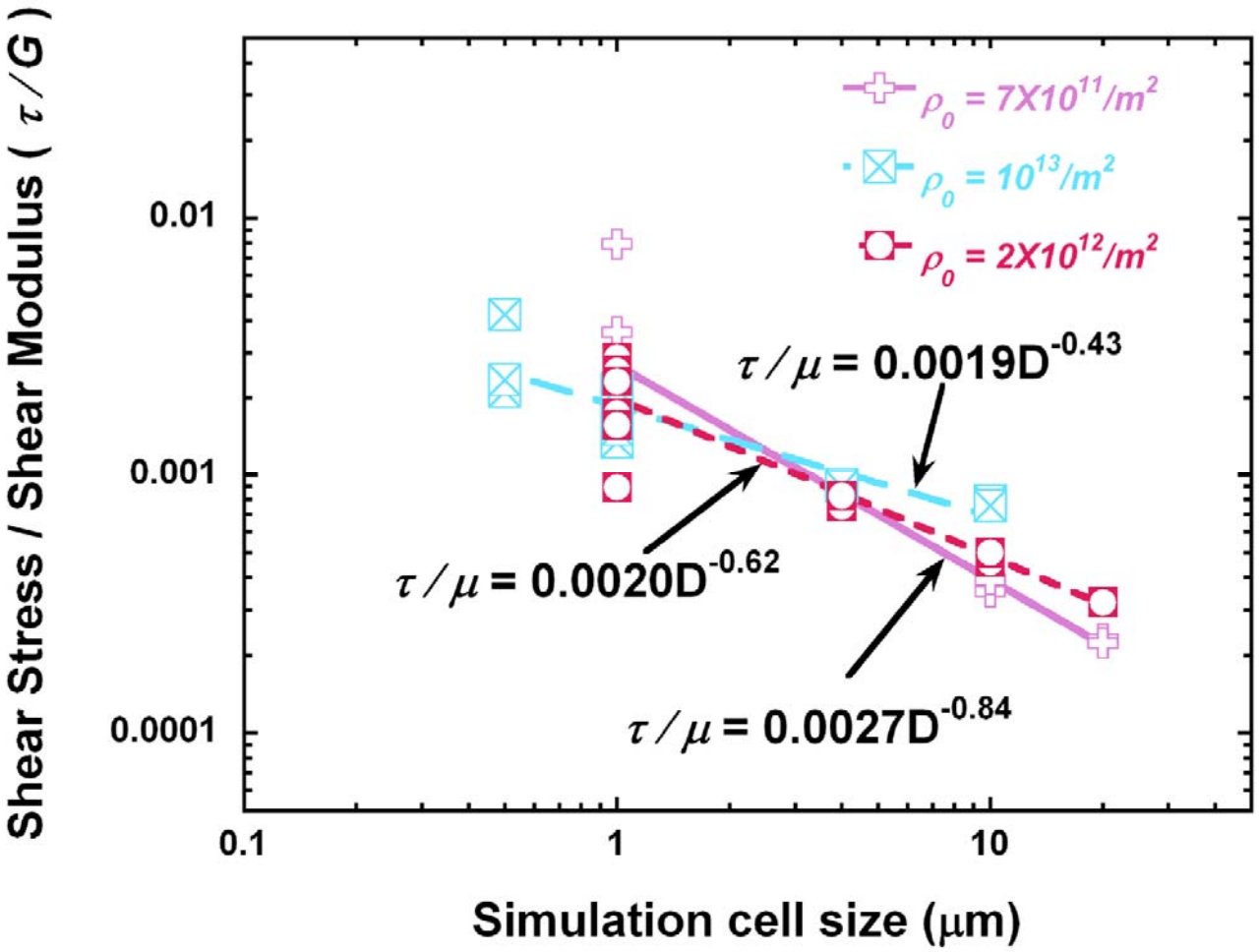
Shear Stress / Shear Modulus (τ / G)
0.01
0.001
0.0001
0.1
1
10
Simulation cell size (μm)
ρ0 = 7X10^11/m^2
ρ0 = 10^13/m^2
ρ0 = 2X10^12/m^2
τ / μ = 0.0019D^-0.43
τ / μ = 0.0020D^-0.62
τ / μ = 0.0027D^-0.84

Fig.7:

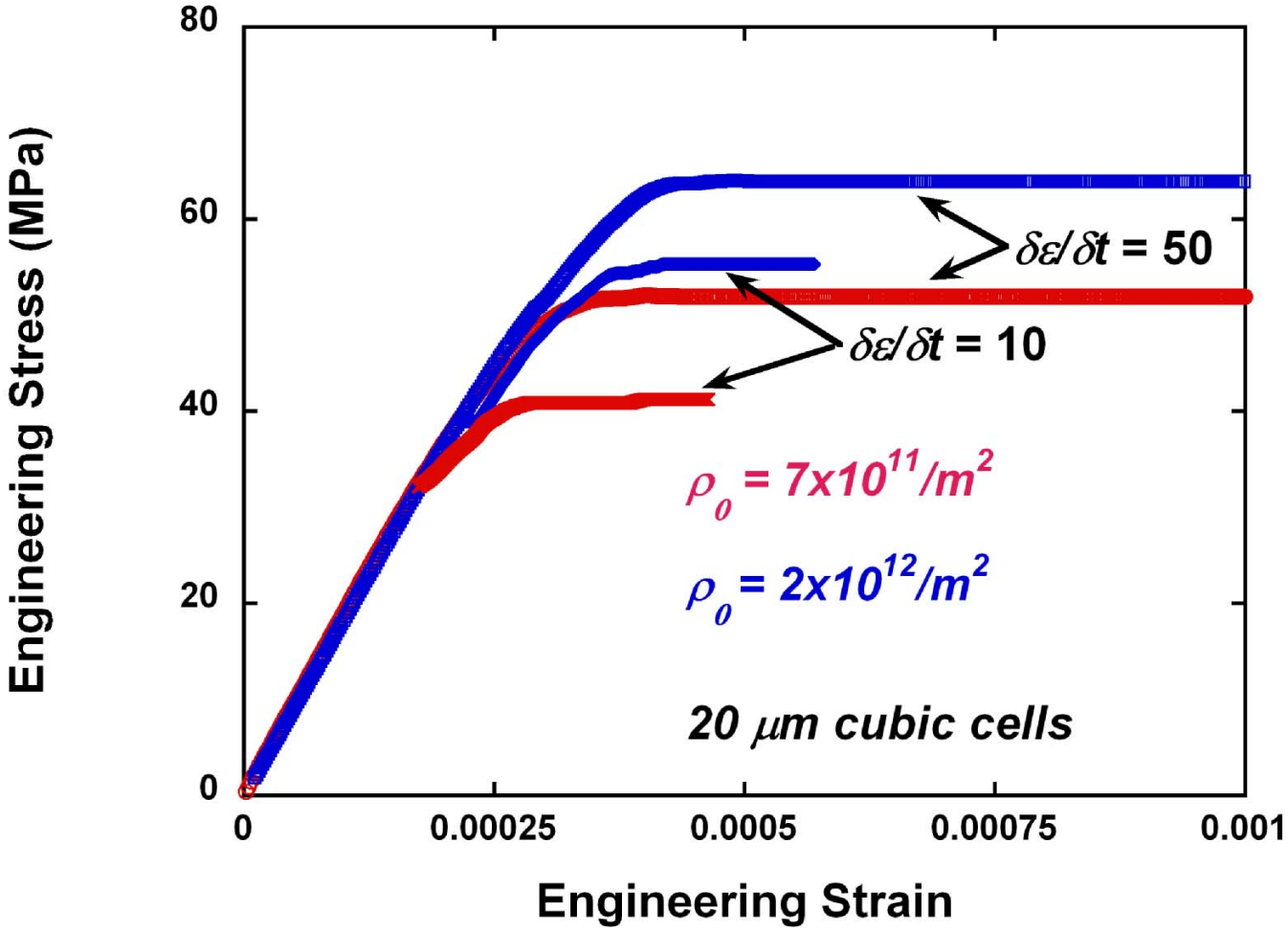
Engineering Stress (MPa)
80
60
40
20
0
0
0.00025
0.0005
0.00075
0.001
Engineering Strain
δε/δt = 50
δε/δt = 10
ρ0 = 7x10^11/m^2
ρ0 = 2x10^12/m^2
20 μm cubic cells

Fig.8:

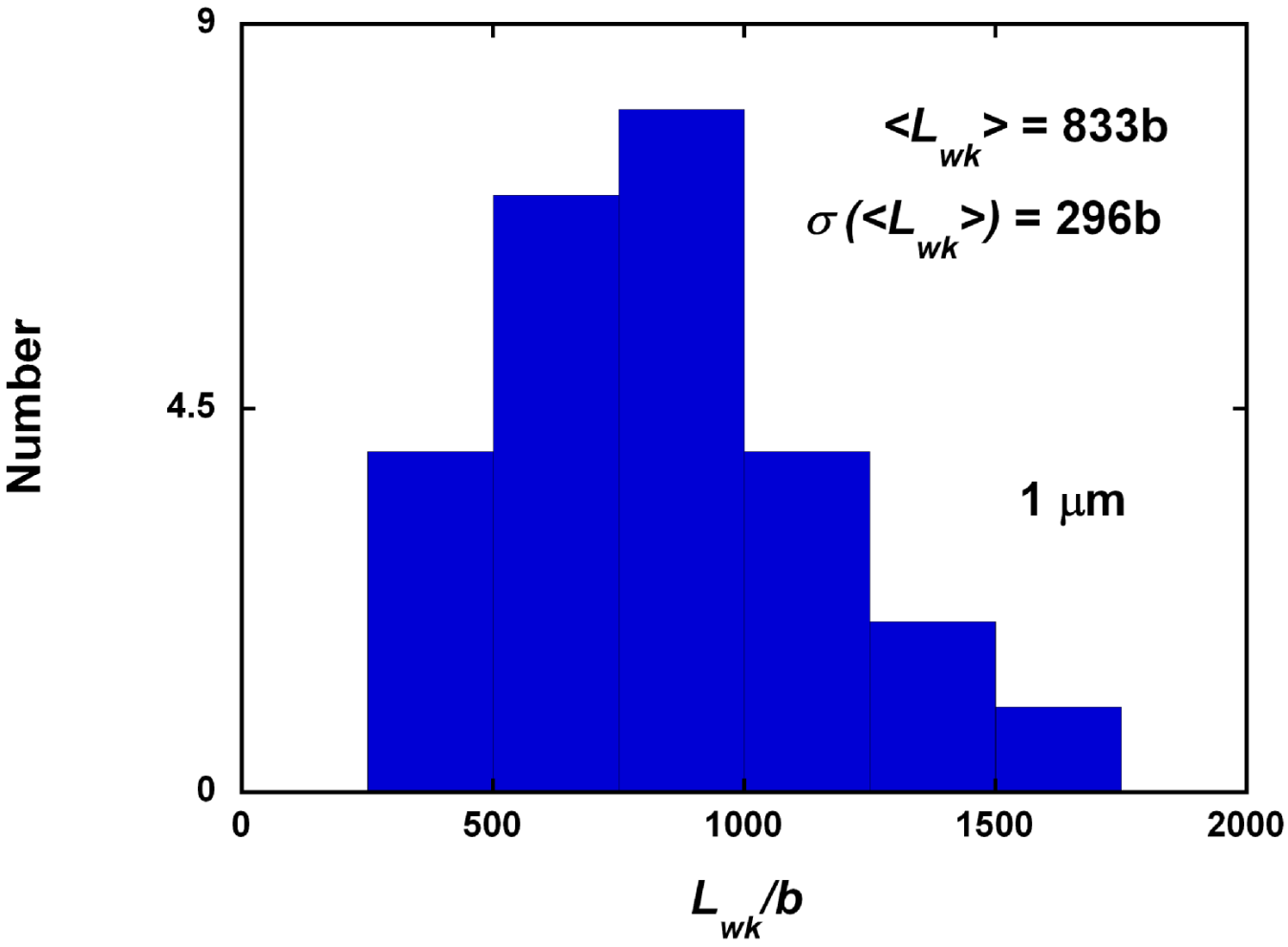
9
4.5
0
Number
0
500
1000
1500
2000
L_{wk}/b
$\langle L_{wk} \rangle$ = 833b
$\sigma(\langle L_{wk} \rangle)$ = 296b
1 μm

Fig.9:

APPENDIX *Further Rationale For Selecting Simulation Parameters*

Initial Source Configurations

The experiments described previously indicate that microcrystal Ni specimens we relief-milled into a mechanically cut, polished and annealed bulk-crystal surface [3]. As such, we envisage that experimental microcrystals initially contain a relatively pinned 3d network of dislocations as a result of the specimen preparation procedures. The initial dislocation density in the microcrystals may range from $5 \times 10^{12}/m^2 - 5 \times 10^{13}/m^2$ [3, 16, 40-42]. During compression testing such microcrystals are flooded with mobile dislocations, most likely from corners or other stress concentrations and perhaps from remaining internal glissile segments. Also, it is well known that "grown-in" dislocations are heavily jogged, in particular if the slip plane is inclined to the surface and the dislocation tends to be normal to the surface of the specimen. If under load the jogs are able to move along the bowing-out dislocations they may condense into a superjogs which then may act as a pinning points [31, 43]. Similarly, pinning points may be introduced on a dislocation segment by the double cross-slip mechanism [31,43] under load.

Ideally, the initial dislocation configurations used in the simulations need to be cut out from an introduced patterned network that is heavily jogged, just as is done for experiments. To produce such initial conditions requires large simulation cells for which the dislocation structure is evolved to large strains. Further, the simulations would need to employ an accurate cross-slip model for accurate production of natural internal sources. However, a reliable procedure for introducing cross-slip into 3d DDS is not yet well established. For example, the cross-slip model that is being used now in 3d DDS literature is specifically developed for the {001} stress axis [66,67]. Ideally, the Friedel-Escaig model of cross-slip for screw-oriented segments in FCC crystals, where the cross-slip activation energy is solely dependent on the local Escaig stresses on the cross-slip and glide planes, respectively, needs to be incorporated into the 3D dislocation dynamics algorithm [68]. Therefore, the present simulations do not include cross-slip thus permitting an examination of purely athermal mechanisms. As a result, we approximate the initial dislocation configuration by a population of FR sources with each FR source having two end pinning points contained within the simulation cell and connected by straight jog-free segments [37].

Aspects pertaining to Loading and the Mechanical State

For the present simulations, the applied external stress is assumed to be uniformly distributed over the volume of the simulation cell. Thus, compressive end effects from misalignment of loading platen and the specimen and the effects of a compliant base, both of which are expected in real experiments, have been neglected in simulation. Under the simulation conditions, dislocations are free to interact with the top and bottom surfaces of the cell in just the same way as for the cell sides. Thus, there is no kinematical constraint from a loading platen or a bulk-crystal base, unlike the experiments.

Strain-gradient effects are largely set aside for the present simulations of microcrystal behavior. This has been done for two reasons. First, the nature of the testing geometry in question is such that in general stretch and bending gradients are negligible in the small strain regime and, very likely also well into the large-strain single-slip regime for many of the experimental tests [3-7]. Note, however, that such experimental conditions not preclude the presence of flow discontinuities (strain gradients), such as those between the rigid crystal base and flowing regions of the crystals found in the experiments. Those gradients are envisaged to be largely of a shear nature, thus being reflected in the dislocations that support the strain rate in the simulations. Second, the current state of development of 3d DDS methods, does not take proper account of lattice rotations (especially locally) and or the storage of excess dislocations that are required to accommodate gradients beyond simple shearing.

As has been pointed out in other studies, proper treatment of free surfaces requires that a traction-free kinematical condition be achieved at the surfaces [9, 13]. However, achieving such conditions are not present computationally feasible for large simulation cells. Thus, a simplified treatment of the surfaces has been developed and employed [19]. For single slip conditions we anticipate that other free-surface mechanical efffects are negligible.